Reconstructing AstroSat UV Deep Field Images

A Thesis

submitted to
Indian Institute of Science Education and Research Pune
in partial fulfillment of the requirements for the
BS-MS Dual Degree Programme

by

Mayank Shekhar Singh

Indian Institute of Science Education and Research Pune
Dr. Homi Bhabha Road,
Pashan, Pune 411008, INDIA.

April, 2025

Supervisor: Prof. Kanak Saha

Certificate

This is to certify that this dissertation entitled Reconstructing AstroSat UV Deep Field Images towards the partial fulfilment of the BS-MS dual degree programme at the Indian Institute of Science Education and Research, Pune represents study/work carried out by Mayank Shekhar Singh at Inter-University Centre for Astronomy and Astrophysics (IUCAA) under the supervision of Prof. Kanak Saha, Professor, during the academic year 2024-2025.

Saha

Prof. Kanak Saha

Committee:

Prof. Kanak Saha

Prof. Susmita Adhikari

Dedicated to my parents...

Declaration

I hereby declare that the matter embodied in the report entitled Reconstructing AstroSat UV Deep Field Images are the results of the work carried out by me at the Inter-University Centre for Astronomy and Astrophysics (IUCAA), Pune, under the supervision of Prof. Kanak Saha and the same has not been submitted elsewhere for any other degree.

Mayank

Mayank Shekhar Singh

Acknowledgments

I would like to express my deepest gratitude to my supervisor, Prof. Kanak Saha, for his invaluable guidance, encouragement, and support throughout this research. His insights and expertise have been instrumental in shaping this work. I sincerely thank Prof. Susmita Adhikari for her time and effort in reviewing my thesis. A special thanks to my seniors in the Galaxy research group, Pushpak Pandey, Manish Kataria, Soumil Maulick, Dr. Anshuman Borgohain, and Dr. Suchira Sarkar, for their continuous support, insightful discussions, and encouragement during the course of this project. Their shared knowledge and experience have been immensely helpful. I would also like to acknowledge the YouTube channel Desi Astro, managed by another one of my group members, Jyoti Prakash, which was helpful in familiarizing me with some of the initial programming concepts used in this work. I also appreciate the guidance and assistance from Dr. Edmund Christian Herenz, whose inputs have been beneficial to this research.

Finally, I extend my heartfelt gratitude to my family and friends, whose unwavering support, patience, and encouragement have been my strongest motivation. Their belief in me has been the foundation of my academic journey, and this work would not have been possible without them.

Abstract

The UltraViolet Imaging Telescope (UVIT) provides a significantly broader Field of View (FOV) than the Hubble Space Telescope (HST); however, this comes at the expense of reduced spatial resolution. This limits the detection of finer structures in the observed images. Our goal is to enhance image resolution by reconstructing these finer details. To achieve this, we apply deconvolution techniques to UVIT images, aiming to recover features that are otherwise blurred by its broad Point Spread Function (PSF) and buried in Poissonian noise. Our approach primarily relies on Maximum Likelihood Estimation (MLE) methods, including the Richardson-Lucy (RL) Deconvolution Algorithm and the Alternating Direction Method of Multipliers (ADMM). First, we model the PSF of UVIT in the Near-Ultraviolet (NUV) and Far-Ultraviolet (FUV) channels and analyze its spatial variation across the field of view. Using synthetic galaxies and stars, we assess the performance of RLTV and ADMM in reconstructing Surface Brightness Profiles and recovery of clumps. We then apply these techniques to real UVIT observations in the GOODS-South field, comparing the results to high-resolution Hubble Space Telescope (HST) images.

Our findings indicate that RLTV preserves photometric accuracy and produces smooth reconstructions, making it suitable for Surface Brightness Profile analysis. In contrast, ADMM better resolves clumpy structures with fewer artifacts but does not conserve flux, limiting its use in photometry. A hybrid approach, leveraging RLTV for photometric studies and ADMM for morphological analysis, may provide an optimal reconstruction strategy. This study demonstrates the effectiveness of hybrid deconvolution techniques in improving UVIT image quality and aiding future deep-field surveys.

Contents

Chapter 1

Introduction

The fascination of humankind with the night sky is millennia-old. Throughout history, philosophers have been trying to understand the fundamental nature of the cosmos. The invention of telescopes was a remarkable achievement to explore deeper into the sky. From identifying the moons of Jupiter by Galileo Galilei in the 17^{th} century to recognizing the Andromeda Nebula (M31) as a galaxy by Edwin Hubble in the early 20th century, astronomical images have been at the center of it all. Stunning snapshots of events that occurred millions of years ago provide us with rich information about the processes taking in those epochs of time. The structures of galaxies, nebulae, and star clusters allow us to study the dynamics and evolution of the observable universe and its components over cosmic history. Space telescopes enable the observation of fainter and more distant objects, providing a deeper look into the universe's past. Deep Field images taken with state-of-the-art telescopes, including the James Webb Space Telescope (JWST) and the Hubble Space Telescope (HST), enable the observation of high-redshift objects ($z \gtrsim 3$) at high resolution and offer insights into galaxy formation and evolution in the early Universe.

The weight and the corresponding expenditure related to space telescopes considerably limit the apertures of these telescopes. Several ground-based telescopes have apertures exceeding 8 meters, whereas the Hubble Space Telescope (HST), one of the largest space-based observatories, has a comparatively smaller aperture of 2.4 meters. For comparison, the Ultraviolet Imaging Telescope (UVIT) aboard ISRO's Astrosat mission (Kumar et al., 2012) has an aperture of 0.375 meters. This limitation in the aperture of the primary mirror leads to a tradeoff between resolution and Field of View (FOV). Higher magnification gives a better resolution and allows us to study finer details of the structure of the celestial objects. However, this narrows the FOV. In the case of HST, particularly the UVIS WFC3 Imaging Camera has an FOV of $\sim 2.5 \times 2.5$ minute^2. On the other end, lower magnification gives us lesser details but a broader FOV, as in UVIT, which has a circular FOV with a diameter of 28 minutes. If the mission aims to cover a larger portion of the sky while it's operational, an FOV can be prioritized at the cost of reduced resolution. This allows these telescopes to cover a much broader part of the sky and uncover more numbers of objects in the sky.

Deconvolution techniques are employed to enhance image resolution by recovering finer details from observations made with telescopes affected by optical limitations. In this thesis, we utilize the Richardson-Lucy (RL) and Alternating Direction Method of Multipliers (ADMM) deconvolution techniques to extract finer features from images captured by the UltraViolet Imaging Telescope (UVIT) in its Far and Near UV bands. This chapter outlines the research problem and provides a review of relevant literature in the field. Before that, we describe the property that defines the resolution of a telescope.

1.1 Point Spread Function

Point Spread Function or PSF (Infante-Sainz et al., 2020) is the response of an imaging device to the light from a point source. For any captured image, it leads to a blurring in the final observation. The origin of PSF lies in the wave property of light. Wave diffraction causes even an ideal point source to appear as an extended intensity distribution rather than a single point. The diffraction limit of an optical device depends on its aperture (D) and the wavelength (λ) of incident light, given by:

$$\theta \approx 1.22 \frac{\lambda}{\mathrm{D}} \tag{1.1}$$

Imperfections in the device, like aberrations, also distort the image. For ground-based telescopes, the Core of the PSF is also dependent on atmospheric conditions and air turbulence during observations. The charge-coupled devices (CCDs) used for imaging further limit the resolution due to pixelation, which adds discreteness to the continuous signal and introduces sampling constraints. The dust particles on the mirror surface cause the PSF to have an extended structure beyond the core, which are referred to as wings or pedestals. In modeling such effects, an exponential profile is frequently employed.

In observational astronomy, bright stars act as a near-perfect point source. This makes modeling of the PSF much simpler. One can construct the Surface Brightness Profile (SBR) of a star image or a stack of star images can be used to model the PSF of the telescope. A PSF model can be constructed using DAOPHOT (Stetson, 1987) program. Another alternative is to construct an effective PSF (ePSF) proposed by Anderson and King, 2000, which is useful for astrometry purposes. In this work, we use Ellipse Task (Jedrzejewski, 1987) to model a two-dimensional PSF by fitting elliptic isophotes.
In the subsequent section, we examine the central research problem of this thesis, which pertains to the deconvolution process.

1.2 Research Problem

Let $\mathbf{x}$ be the intrinsic image of an object captured by the camera and $\mathbf{P}$ represent the PSF of the telescope, the observed image $\mathbf{y}$ is given by:

$$\mathbf{y}(i,j) = (\mathbf{P} \circledast \mathbf{x})(i,j) + \eta(i,j) \tag{1.2}$$

where $\circledast$ represents a convolution operation, (i,j) is the corresponding pixel, and η refers to the noise.
This convolution operation results in image blurring, making it challenging to detect fine structures when $\mathbf{P}$ is broad. Our objective is to apply deconvolution to reconstruct the intrinsic image $\mathbf{x}$ from the observed image $\mathbf{y}$, enabling the recovery of fainter features in the objects.
The noise or sky background in UVIT images follows Poissonian statistics (Saha, Maulick, et al., 2024), where the noise at pixel i is governed by the relation:

$$p(\mathbf{y}_i|\mathbf{x}) = \frac{(\mathbf{P} \circledast \mathbf{x})_i^{\mathbf{y}_i} e^{-(\mathbf{P} \circledast \mathbf{x})_i}}{\mathbf{y}_i!} \tag{1.3}$$

The objective is to employ deconvolution algorithms that explicitly account for Poissonian noise in the reconstruction of source images.
In general, Equation 1.2 represents an ill-posed problem, meaning it lacks a unique or stable solution. The various deconvolution algorithms discussed in the following section provide different approaches to constructing the 'best estimate' of the source.

1.3 Deconvolution Methods

In the absence of noise, the deconvolution problem simplifies to taking a Fourier transform $\mathscr{F}\cdot$ (Bracewell, 2000), performing a division in the frequency domain, and applying an inverse transform ($\mathscr{F}^{-1}\cdot$) to recover the intrinsic image.

$$\mathscr{F}\{\mathbf{y}\} = \mathscr{F}\{\mathbf{P}\} \cdot \mathscr{F}\{\mathbf{x}\} \Rightarrow \mathbf{x} = \mathscr{F}^{\mathbf{-1}}\left\{\frac{\mathscr{F}\{\mathbf{y}\}}{\mathscr{F}\{\mathbf{P}\}}\right\} \tag{1.4}$$

Here, $(\cdot)$ and $(/)$ denote an element-wise multiplication and division, respectively.
This method is referred to as the Fourier Quotient Method. However, in the presence of noise, as is the case with all astronomical images, this method introduces significant artifacts that make feature recovery impossible. The main issue arises from the cutoff frequency of the PSF, where the division in the Fourier domain amplifies noise at frequencies close to the cutoff, causing severe degradation of the reconstructed images.
A widely used method used in Radio Astronomy is CLEAN (Högbom, 1974), which assumes that the intrinsic image consists solely of point sources. While effective for sparse distributions, it performs poorly when reconstructing extended sources. Another commonly used approach is the Maximum Entropy Method (MEM) (Frieden, 1978; Cornwell and Evans, 1985), which formulates image reconstruction as an entropy maximization problem, providing better results for diffuse structures.
In the context of a sky background that follows Poissonian statistics (given in equation 1.3), a popular method used is the Classical Richardson-Lucy Algorithm (CRLA) (Richardson, 1972; Lucy, 1974). It is a Maximum Likelihood Estimate (MLE) algorithm. The main advantage of using this is the preservation of flux and positive values in the reconstructed image. This algorithm also suffers from speckling or noise amplification due to violating the Nyquist Sampling Theorem (Nyquist, 1928). To avoid this issue, in our work, we have used a modification to the existing CRLA proposed by Nkashima and Takami, 1999 referred to as the Modified Richardson Lucy Algorithm (MRLA). Another cause of noise amplification is due to the problem being ill-posed. Adding a regularization parameter or a prior: Total Variation (Rudin et al., 1992; Dey et al., 2006; Sakai et al., 2023) converts the problem to now a Maximum a Posteriori (MAP) estimation. This method reduces noise amplification by imposing smoothness constraints.
Another way to solve optimization problems is by using the Alternating Direction Method of Multipliers (ADMM)(Boyd et al., 2011). ADMM is extensively studied in image processing

and the reconstructed images are more robust to artifacts. The specific ADMM formulation used in this work follows the approaches outlined in Shibuya et al., 2022; Figueiredo and Bioucas-Dias, 2010.

More details about the deconvolution algorithms discussed above and many others, including wavelet analysis and sparse modeling, are available in Starck et al., 2002.

1.4 Thesis Outline

The structure of this thesis is organized as follows:

Chapter 2 provides a detailed description of the data used in this project, including its sources, characteristics, and relevance to the study. Chapter 3 presents the methodology for modeling the PSF of the UVIT telescope, outlining the preprocessing steps and modeling techniques employed to characterize the system's optical response. Chapter 4 introduces the deconvolution framework, describing the Richardson-Lucy (RL) and Alternating Direction Method of Multipliers (ADMM) algorithms, along with the step-by-step procedures for image reconstruction. Chapter 5 discusses the results obtained from the reconstructed images, providing a comprehensive analysis of the effectiveness of the methods in enhancing resolution. Finally, Chapter 6 summarizes the key findings of this work and explores their implications for future research in image restoration and analysis.

Chapter 2

Data Sources

Ultraviolet Astronomy plays a crucial role in studying various phenomena including Galaxy Formation, Active Galactic Nuclei, IGM, CGM, etc. Since most of the UV light is absorbed by the Earth's atmosphere, the only way to get scientific-grade UV images is through telescopes aboard satellites orbiting the Earth. In our work, UV images from UVIT and HST have been used. In this chapter, we examine the specifications of the telescopes used and provide a detailed description of the images utilized in this thesis.

2.1 Telescopes

2.1.1 UVIT

The Ultra Violet Imaging Telescope (Kumar et al., 2012) on ASTROSAT Satellite is a multi-wavelength mission by the Indian Space and Research Organization (ISRO). It operates in three bands: Far-Ultraviolet (FUV: 1300 - 1800 Å), Near-Ultraviolet (NUV: 2000 - 3000 Å), and Visible (VIS: 3200 - 5500 Å) with a Field of View of diameter ~ 28 arc-minutes. The VIS channel is primarily used for calibration purposes including alignment and drift measurement. We have used images taken in the FUV (F154W) and NUV (N242W) filters of the telescopes. The pixel scale in images of both the filters is 0.417".

2.1.2 HST

The Hubble Space Telescope (HST), since its launch in 1990, has revolutionized our understanding of the universe. It operates in quite a broad range of the electromagnetic spectrum from ultraviolet to infrared (1150 – 25000 Å). This project, in particular, utilizes data observed with the Wide Field Camera (WFC3) on Hubble in the UVIS channel sensitive to the UV and Optical bands. In particular, we use images taken with F275W (2200 - 3120 Å) and F336W (3000 - 3700 Å) filters. The pixel scale in these two filters is 0.06".

2.2 Observation

In this work, we utilize the AstroSat UV Deep Field South (AUDFs) (Saha, Maulick, et al., 2024) imaging survey. The data used here has been surveyed from Chandra Deep Field South (ObsID: GT05-240, PI: Kanak Saha) about two points, CDFS-I ((53.03394, -27.91539) and CDFS-II (53.25806, -27.68067) of exposure time ~ 31 ks each (shallow region), such that their FOV ($\sim 28'$ diameter) has an overlapping region that contains the Great Observatories Origins Deep Survey (GOODS) South field with exposure time of ~ 62 ks (deep region). These observations were done simultaneously in the F154W and the N242W filters. The FUV and NUV observations were done in Photon Counting mode with a frame rate of 28.7 per second. The photometric zero-points for F154W and N242W are 17.77 and 19.76, respectively (Tandon, Postma, et al., 2020) in the AB magnitude system.
We use images from the public data of Hubble Legacy Fields (HLF) V2.0 GOODS-S Photometric Catalog (Whitaker et al., 2019) from the HST archival program AR-13252. The coverage details of HST coverage and UVIT coverage can be found in (Saha, Maulick, et al., 2024). The exposure times for the two filters is ~ 210 ks. The photometric zero-points for the F275W and F336W filters are 24.13 and 24.67, respectively. The images from HST are only used for reference to the images reconstructed by deconvolution of the UVIT images.

2.2.1 Sample Selection of Stars for PSF Modeling

A total of 93 GAIA stars (Gaia Collaboration et al., 2021) in NUV and 59 GAIA stars in FUV are identified. These stars were extracted as a cutout of 171×171 pixels from the

whole field, and science-ready images were extracted by dividing the photon-counting images with their corresponding exposure time maps. The stars were cross-checked against the GAIA catalog to eliminate any double stars. Any stars significantly contaminated by nearby sources and those too faint to model a PSF were also not considered. A few bright stars from the NUV filter were ignored for having a significant saturation effect.
A total of 77 stars in the NUV field and 10 stars in the FUV field, were found appropriate to model their Point Spread Function. The faintest suitable stars had the maximum magnitude of ~ 23.21 and ~ 22.71 for NUV and FUV, respectively.

This chapter provides an overview of the data used in our analysis, including observations from UVIT and relevant archival HST datasets. Before addressing deconvolution, it is essential to construct an accurate PSF model, which we detail in the next chapter.

Chapter 3

PSF Modeling

Modeling the Point Spread Function is an essential requirement for any photometric analysis. To compare any features of an object obtained from different instruments, without correcting for PSF would produce incorrect results. It is an important feature for calculating Source to Noise Ratio (SNR), and modeling Spectral Energy Distributions (SEDs) and Luminosity Profiles among other things. In this chapter, we discuss the process of modeling a PSF from the star cutouts obtained in 2.2.1.

3.1 Background Estimation

Background estimation is a crucial step for photometry. Any analysis using the image data requires a background-subtracted image. There are several methods to measure and estimate the sky background in a fits image file. Here, the image cutouts for the stars are small enough to assume no variation in the sky background across the image.

The simplest is to measure a median; however, it grossly overestimates the value as the pixels from sources are included in the measurement. A better method is σ-clipping, which involves computing statistics of all the pixel values and then excluding pixels with values beyond 3σ (convention) from the mean. This procedure is repeated till convergence or till a specified number of iterations has been reached. However, this process may not be able to accurately estimate the background in a crowded field or with faint sources present in the field.

The approach we use here for estimating the background is to place semi-random boxes (Rafelski et al., 2015), avoiding sources, i.e., `SExtractor` segmented pixels. In each cutout, 150 non-overlapping boxes of dimensions 7×7 pixel^2 are placed, and mean and standard deviation (or RMS) are computed for each box. A histogram of the statistics from one such star cutout is given in Figure 3.1. As the Histogram appears to be following a Gaussian curve, the mean of this distribution is taken as the estimate of the sky background for the corresponding cutout. We subtract the mean background calculated in this step from any images used in photometry.

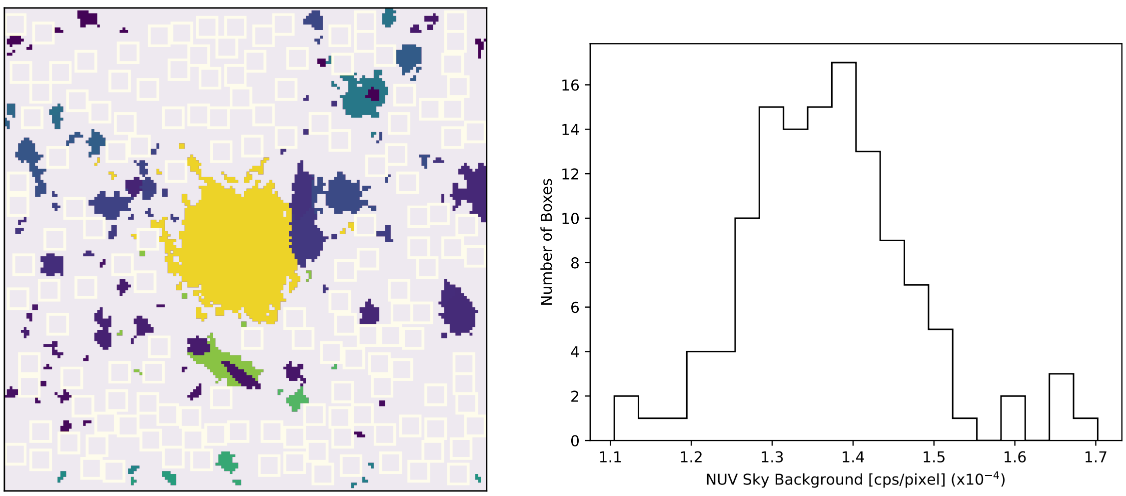

Figure 3.1: Estimation of background using Semi-random boxes. **a)** 150 Boxes of size 7×7 pixel^2 on a star observed in NUV filter. **b)** A histogram of the mean value measured in the boxes.

3.2 Cleaning

Cleaning is an essential part of the procedure in PSF modeling. Faint contaminants can affect the modeling of the profile, especially for the extended wings of the PSF. The `SExtractor` segmentation map for each cutout is used to identify the contaminants. In this work, instead of replacing the pixels marked from the segmented map with background noise from nearby pixels, the pixel data is replaced by a random value from an annulus around the star of thickness 3 pixels at the same radius. We construct a set of valid pixels inside this annulus that do not belong to any source segmentation map except for the central star. The pixel is then replaced by a random pixel value from this set. This prevents the pixels that might be a part of the extended wings from being replaced by a lower sky background value.

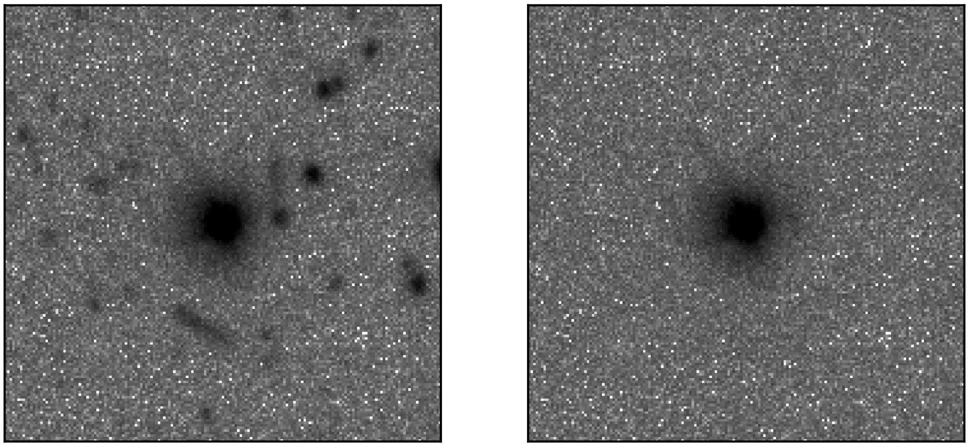

Figure 3.2: Cleaning of images to remove any contaminant from the surroundings of the central star.

3.3 Saturation Correction

In photon counting mode, multiple photon events in close vicinity (3×3 pixel^2) in a frame are recorded as a single photon event. In bright stars, therefore, a saturation correction is required, which may affect the modeling of the core of the PSF and may lead to a wrong estimate of the FWHM.

All the stars with total flux ≥ 1 are considered for saturation correction. The actual counts/frame can be estimated using the Poissonian statistics relation. However, the PSF spreads more than 3×3 pixel^2, so an empirical procedure (Tandon, Postma, et al., 2020; Devaraj et al., 2023) described below is used. Let's assign CPF5 as the 97% of observed counts per frame, and ICPF5 would be the actual count per frame by Poissonian statistics. The correction to counts per frame is given as follows:

$$\mathrm{CPF5} = 1 - exp(-\mathrm{ICPF5}) \tag{3.1}$$

$$\mathrm{ICORR} = \mathrm{ICPF5} - \mathrm{CPF5} \tag{3.2}$$

$$\mathrm{RCORR} = \mathrm{ICORR} \times (0.89 - 0.30 \times (\mathrm{ICORR})^2) \tag{3.3}$$

Where ICORR is the ideal correction, and RCORR is the real correction. Moreover, CPF5 can be estimated from total counts in a window of radius ~ 29 pixels, which accounts for 97% of the total counts.
No FUV stars showed any saturation, and hence, no correction was applied. A few of the brightest NUV stars showed significant saturation beyond correction, causing a dip around the central peak in the image similar to an observation discussed in Tandon, Hutchings, et al., 2017 at a radius of ~ 10 pixels, which alters the surface brightness profile of the stars. These stars were hence ignored from our sample.

3.4 Ellipse Task

The ellipse procedure (Jedrzejewski, 1987) is an iterative method to fit isophotes. The algorithm begins at a first-guess elliptical isophote defined by approximate center coordinates (X_0, Y_0), ellipticity (ϵ), and position angle (φ) values. Using these values, the image is sampled along an elliptical path, producing a 1-D function that describes the dependence of intensity (pixel values) with angle (θ). This function is then least-squares fitted to

$$I = I_0 + A_1 sin(\theta) + B_1 cos(\theta) + A_2 sin(2\theta) + B_2 cos(2\theta) \tag{3.4}$$

The coefficients A_1, A_2, B_1, B_2 represent fitting errors, which are reduced with each iteration to achieve a correct fit as the following

$$\Delta\text{Major Axis Location} = \frac{-B_1}{I'} \tag{3.5}$$

$$\Delta\text{Minor Axis Location} = \frac{-A_1(1-\epsilon)}{I'} \tag{3.6}$$

$$\Delta\epsilon = \frac{-2B_2(1-\epsilon)}{a_0 I'} \tag{3.7}$$

$$\Delta\varphi = \frac{2A_2(1-\epsilon)}{a_0 I'[(1-\epsilon)^2 - 1]} \tag{3.8}$$

$$\tag{3.9}$$

where I' is the gradient of intensity along the major axis direction calculated at the length of the semi-major axis a_0. The stopping criterion for the best fit is the largest harmonic amplitude to be less than 4% of rms residual of the intensity distribution fitting in equation

3.4. The intensity of these isophotes is also calculated, corresponding to each ellipse, to generate a Surface Brightness Profile (SBR) or a 1-D radial profile for the PSF.
We use this obtained best-fit ellipse to find the higher harmonics for the intensity distribution by doing a least-squares fit to:

$$I = I_0 + A_n sin(n\theta) + B_n cos(n\theta) \tag{3.10}$$

In this work, we only use n = 3,4. These amplitudes are not affected by the first and second harmonics due to orthogonality. The third harmonic amplitudes describe the asymmetry of the ellipse and the fourth order amplitudes describe the boxiness of the isophote.

3.5 Radial Profile

The intensity profiles of bright stars representing the instrumental PSF can be dissected in a central core and an extended wing. We find the combination of a Moffat profile (Moffat, 1969) and an exponential profile (Saha, Dhiwar, et al., 2021) to be suitable for the core.

$$I(r) = I_{c0}\left[1 + \left(\frac{r}{\alpha}\right)^{-\beta}\right] + I_{w0}e^{-r/R_s} \tag{3.11}$$

The Moffat term is used for modeling the core of the PSF while the Exponential term is used for the extended pedestal. The Full Width at Half Maxima (FWHM) of the Moffat core is given by:

$$FWHM = 2\alpha\sqrt{2^{1/\beta} - 1} \tag{3.12}$$

Some fainter stars, however, do not have a sufficient length of the profile to model the pedestal. For these stars, 11 in NUV and 4 in FUV, we model only their cores with the Moffat profile.

Chapter 4

Deconvolution

This chapter presents the Richardson-Lucy (RL) and Alternating Direction Method of Multipliers (ADMM) algorithms for image deconvolution. RL, based on maximum likelihood estimation, iteratively refines the reconstructed image, while ADMM formulates the problem as an optimization task, incorporating regularization for improved artifact suppression. Both methods aim to enhance image resolution and recover fine structural details.

4.1 Classical Richardson Lucy Algorithm

CRLA was developed independently by W.H. Richardson (Richardson, 1972) and Leon B. Lucy (Lucy, 1974) to restore degraded and noisy images. It treats the images, PSF, and the observed images as probability-frequency functions, and the iterative algorithm can be derived using Bayes' Theorem. Here, however, we take a Maximum Likelihood approach to derive the algorithm in the context of Poissonian Noise to solve for $\mathbf{x}$ in equation 1.2.

Let $\mathbf{y}$ be the observed image, $\mathbf{P}$ be the PSF, and $\mathbf{x}$ represent the reconstructed image. The noise follows the Poissonian relation at a specific image pixel i given by

$$p(\mathbf{y}|\mathbf{x}) = \frac{(\mathbf{P} \circledast \mathbf{x})^{\mathbf{y}} e^{-(\mathbf{P} \circledast \mathbf{x})}}{\mathbf{y}!} \tag{4.1}$$

It can be formulated into a maximum likelihood optimization problem by defining a `-log` Lagrangian or the fidelity term as

$$\mathcal{L}(\mathbf{y},\mathbf{x}) = -\log\left(\frac{(\mathbf{P}\circledast\mathbf{x})_i^{\mathbf{y}_i} e^{-(\mathbf{P}\circledast\mathbf{x})_i}}{\mathbf{y}_i!}\right) \tag{4.2}$$

We can now define our optimization problem as

$$\mathbf{x} := \min_{\{\mathbf{x}\}} \; \mathcal{L}(\mathbf{y},\mathbf{x}) + \lambda T(\mathbf{x}) \tag{4.3}$$

where $\mathbf{T(x)}$ is a `Prior` term and λ acts a parameter to balance the two terms. This inclusion of a prior changes the problem to a maximum a posteriori one as in Bayesian inference.
For CRLA, we do not assume a prior and thus proceed with $\lambda = 0$. From the equations 4.2 and 4.3, we have

$$\mathbf{x} := \min_{\{\mathbf{x}\}} \; \mathbf{P}\circledast\mathbf{x} - \log(\mathbf{P}\circledast\mathbf{x})\cdot\mathbf{y} \tag{4.4}$$

Differentiating the previous equation w.r.t $\mathbf{x}$ gives us:

$$\begin{aligned} \mathbf{1}\circledast\mathbf{P}^T - \frac{\mathbf{y}}{\mathbf{P}\circledast\mathbf{x}}\circledast\mathbf{P}^T &= 0 \\ \mathbf{1} = \frac{\mathbf{x}^{t+1}}{\mathbf{x}^t} &= \frac{\mathbf{y}}{\mathbf{P}\circledast\mathbf{x}}\circledast\mathbf{P}^T \end{aligned} \tag{4.5}$$

where $\mathbf{1}$ is an all-one image, $\mathbf{P}^T$ is the transpose of the PSF matrix and $\mathbf{t}$ is the iteration index. Here we use the result $\mathbf{1}\circledast\mathbf{P} = \mathbf{1}$ if $\mathbf{P}$ is a positive normalized matrix. Hence, the iterative algorithm for the Classical Richardson-Lucy Algorithm is given by

$$\mathbf{x^{t+1}} = \mathbf{x^t}\cdot\left(\frac{\mathbf{y}}{\mathbf{P}\circledast\mathbf{x^t}}\circledast\mathbf{P^T}\right) \tag{4.6}$$

For any non-negative initial guess, i.e., $\mathbf{x}^0 \geq 0$, the value will remain positive in all following iterations.
The simplicity of implementing this algorithm is one of its features. It can be easily proven that by using a normalized PSF, the total flux is conserved in each iteration. The astronomical images reconstructed show a super-resolution effect due to the increase in the Spatial Cutoff Frequency during the maximum likelihood estimation.

The CRLA, however, leads to artifacts and ringing effects. The primary reason for this phenomenon is the violation of the Nyquist Sampling Theorem (Nyquist, 1928) by the algorithm and the convergence of CRLA not necessarily leading to a global maximum due to it being an ill-posed problem. In the next section, we discuss a modified version of the CRLA that deals with the first problem.

4.2 Modified Richardson Lucy Algorithm

According to the Nyquist Theorem, the PSF of an image should occupy nearly 3×3 pixel grid (Li et al., 2024). The typical FWHM of the PSF in instruments is 2-4 pixels, i.e., in accordance with the sampling theorem. With deconvolution, the resolution increases with iterations and hence, it would violate the sampling theorem. To avoid this, we can use the method proposed by Nkashima and Takami, 1999: Modified Richardson Lucy Algorithm (MRLA). We interpolate the image to a suitable scale and instead of the original observed PSF ($\mathbf{P}$), we use a sub-pixeling narrower function $\mathbf{S}$. The two are related by the following:

$$\mathbf{P} = \mathbf{R} \circledast \mathbf{S} \tag{4.7}$$

Where $\mathbf{R}$ is an appropriate PSF at the pixel scale of the interpolated image chosen by us. We can determine $\mathbf{S}$ by the Fourier-Quotient Method (1.4) and using a suitable window to remove high-frequency noise.
Now, the image equation (1.2) can be redefined as:

$$\begin{aligned} \mathbf{y} &= (\mathbf{R} \circledast \mathbf{S}) \circledast \mathbf{x} + \eta \\ &= \mathbf{S} \circledast (\mathbf{R} \circledast \mathbf{x}) + \eta \\ &= \mathbf{S} \circledast \mathbf{z} + \eta \end{aligned} \tag{4.8}$$

This can be solved similarly to the CRLA algorithm to give:

$$\mathbf{z^{t+1}} = \mathbf{z^t} \cdot \left(\frac{\mathbf{y} + \mathbf{C}}{\mathbf{S} \circledast \mathbf{z^t} + \mathbf{C}} \circledast \mathbf{S^T} \right) \tag{4.9}$$

where C is a positive constant to maintain the non-negativity of the problem and prevent any divisions with very small numbers or zeros. In our case, we observe that the UVIT pixel scale (0.417") $\sim 7\times$ HST pixel scale (0.06"). Hence, the image is interpolated to a scale of 7 times its original size. The original PSF $\mathbf{P}$ is redefined on this scale, and a suitable PSF $\mathbf{R}$ is chosen, which is similar in shape to the original PSF profile, to avoid any Spectral leakage. Some artifacts still persist in the deconvolved images due to the inherently ill-posed nature of the deconvolution problem. To address those, we add a Total Variation Prior to our algorithm.

4.3 RL with Total Variation Prior

Total Variation or TV prior (Rudin et al., 1992) is a regularization that reduces noise amplification by imposing a smoothness constraint. It can be added in the equation 4.3 as:

$$\mathbf{x} := \min_{\{\mathbf{x}\}} \mathcal{L}(\mathbf{y}, \mathbf{x}) + \lambda \ \mathrm{TV}(\mathbf{x}) \tag{4.10}$$

where for TV function we use the L_1 norm over $\nabla \mathbf{x}$. This also makes it a maximum a posteriori (MAP) estimation problem. The derivation of the algorithm is similar to CRLA (Dey et al., 2006; Sakai et al., 2023). The iterative algorithm with TV prior is given by:

$$\mathbf{x^{t+1}} = \frac{\mathbf{x^t}}{\mathbf{1} - \lambda \ \mathrm{div}\left(\frac{\nabla \mathbf{x^t}}{|\nabla \mathbf{x^t}|}\right)} \cdot \left(\frac{\mathbf{y}}{\mathbf{P} \circledast \mathbf{x^t}} \circledast \mathbf{P^T}\right) \tag{4.11}$$

where $\mathrm{div}(\cdot)$ is the divergence. The regularization parameter (λ) is to not be chosen too small or large. For very small values of λ, it would revert back to the CRLA and for values ~ 1, the algorithm may become unstable. We determine that $\lambda = 0.0002$ is an appropriate regularization parameter, as it preserves fine details while avoiding excessive smoothing in the reconstructed image. To preserve the total flux, the last iteration is run without the TV correction. In this work, we combine the TV prior with the MRLA to further reduce the artifacts.

4.4 Alternating Direction Method of Multipliers

ADMM is a technique that handles convex optimization problems by breaking them into smaller, simpler problems. This method addresses the problems of the form

$$\begin{aligned} \text{minimize} \;\; & f(x) + g(z) \\ \text{subject to} \;\; & Ax + Bz = C \end{aligned}$$

where f, g functions are assumed to be convex functions and $x \in \mathbb{R}^n, z \in \mathbb{R}^m, A \in \mathbb{R}^{p\times n}, B \in \mathbb{R}^{p\times m}, C \in \mathbb{R}^p$. The solution is then defined as

$$p^* = \inf\ \{f(x) + g(z) | Ax + Bz = C\} \tag{4.12}$$

We define an augmented Lagrangian to split this problem into smaller parts.

$$\mathcal{L}_\rho = f(x) + g(z) + h^T(Ax + Bz - C) + \frac{\rho}{2}||Ax + Bz - C||_2^2 \tag{4.13}$$

Here, **h** is the Lagrangian multiplier, ρ is the penalty parameter and $||\cdot||_2^2$ represents an L_2 norm. This problem given in 4.12 is solved iteratively by updating **x**, **z**, and **h**.

$$x^{k+1} := \text{argmin}\ \ \mathcal{L}_\rho(x, z^k, h^k) \tag{4.14}$$

$$z^{k+1} := \text{argmin}\ \ \mathcal{L}_\rho(x^{k+1}, z, h^k) \tag{4.15}$$

$$h^{k+1} := h^k + \rho(Ax^{k+1} + Bz^{k+1} - C) \tag{4.16}$$

The details of ADMM and its various applications can be found in Boyd et al., 2011.

4.4.1 Applying ADMM to Image Restoration

The problem of image restoration using ADMM (Shibuya et al., 2022; Figueiredo and Bioucas-Dias, 2010) can be described using the Poissonian statistics and by combining two penalty functions

$$\underset{\{\mathbf{x}\}}{\text{minimize}}\ \ -\log[p(\mathbf{y}|\mathbf{w}_1)] + I_{R_+}(\mathbf{w}_2) \tag{4.17}$$

$$\text{subject to } \mathbf{Ax} - \mathbf{w} = 0$$

Here, $\mathbf{y}$ represents the observed image, $\mathbf{x}$ is the reconstructed image, $\mathbf{P}$ is the Point Spread Function matrix of the telescope, and $p(\mathbf{y}|\mathbf{x})$ is the Poissonian distribution as in 4.1. We define $\mathbf{A}$ and $\mathbf{w}$ as

$$\mathbf{A} = \begin{bmatrix} \mathbf{P} \\ \mathbf{I} \end{bmatrix}, \quad \mathbf{w} = \begin{bmatrix} \mathbf{w}_1 \\ \mathbf{w}_2 \end{bmatrix}$$

$\mathbf{I}$ is the identity matrix. The first term in the equation 4.17 is the log-likelihood estimator, and the second term is an indicator function given by

$$I_{R_+}(w) = \begin{cases} 0 & w \in R_+ \\ +\infty & w \notin R_+ \end{cases} \tag{4.18}$$

where R_+ is the closed non-empty convex set implying the non-negativity constraints. The $\mathbf{w}_1$ and $\mathbf{w}_2$ are auxiliary variables introduced here for the terms of Poissonian noise and flux non-negativity, respectively.

The Augmented Lagrangian for the defined optimization problem, following from the equation 4.13, can be written as

$$\mathcal{L}_\rho(\mathbf{x}, \mathbf{w}, \mathbf{h}) = -\log[p(\mathbf{y}|\mathbf{w}_1)] + I_{R_+}(\mathbf{w}_2) + \mathbf{h}^T(\mathbf{A}\mathbf{x} - \mathbf{w}) + \frac{\rho}{2}||\mathbf{A}\mathbf{x} - \mathbf{w}||_2^2 \tag{4.19}$$

The reconstruction problem is divided into three sub-problems: PSF convolution, Poissonian noise, and flux non-negativity. Here, we use instead a scaled Lagrange multiplier defined as $\mathbf{u} := (1/\rho)\mathbf{h}$. The sub-problems are solved using the proximal operator to update $\mathbf{x}$ iteratively, $\mathbf{w}_1$, $\mathbf{w}_2$, and $\mathbf{u}$ as following

$$\begin{aligned}
\mathbf{x} \leftarrow \mathbf{prox}_q(\mathbf{v}) &= \underset{\{\mathbf{x}\}}{\operatorname{argmin}} \ \mathcal{L}_\rho(\mathbf{x}, \mathbf{w}, \mathbf{h}) \\
&= \underset{\{\mathbf{x}\}}{\operatorname{argmin}} \ \frac{1}{2}||\mathbf{A}\mathbf{x} - \mathbf{v}||_2^2, \\
\mathbf{v} &= \mathbf{w} - \mathbf{u} \\
\mathbf{w}_1 \leftarrow \mathbf{prox}_{\mathrm{p},\rho}(\mathbf{v}) &= \underset{\{\mathbf{w}_1\}}{\operatorname{argmin}} \ \mathcal{L}_\rho(\mathbf{x}, \mathbf{w}, \mathbf{h}) \\
&= \underset{\{\mathbf{w}_1\}}{\operatorname{argmin}} \ -\log[p(\mathbf{y}|\mathbf{w}_1)] + \frac{\rho}{2}||\mathbf{v} - \mathbf{w}_1||_2^2,
\end{aligned} \tag{4.20}$$

$$\mathbf{v} = \mathbf{P}\mathbf{x} + \mathbf{u}_1 \tag{4.21}$$

$$\begin{aligned}\mathbf{w}_2 \leftarrow \mathbf{prox}_{\mathrm{i},\rho}(\mathbf{v}) &= \underset{\{\mathbf{w}_2\}}{\operatorname{argmin}}\ \mathcal{L}_\rho(\mathbf{x},\mathbf{w},\mathbf{h}) \\ &= \underset{\{\mathbf{w}_2\}}{\operatorname{argmin}}\ I_{R_+}(\mathbf{w}_2) + \frac{\rho}{2}||\mathbf{v} - \mathbf{w}_2||_2^2,\end{aligned}$$

$$\mathbf{v} = \mathbf{x} + \mathbf{u}_2 \tag{4.22}$$

$$\begin{bmatrix} \mathbf{u_1} \\ \mathbf{u_2} \end{bmatrix} \leftarrow \mathbf{u} + \mathbf{A}\mathbf{x} - \mathbf{w} \tag{4.23}$$

Now, we discuss the proximal operators used in the ADMM procedure for deconvolution.

Quadratic Sub-problem: $\mathbf{prox}_q$

We now describe the proximal operator for the $\mathbf{x}$ update, which solves a quadratic problem.

$$\begin{aligned}\mathbf{prox}_q(\mathbf{v}) &= \underset{\{\mathbf{x}\}}{\operatorname{argmin}}\ \frac{1}{2}||\mathbf{A}\mathbf{x} - \mathbf{v}||_2^2 \\ &= \underset{\{\mathbf{x}\}}{\arg\min} \frac{1}{2}\left|\left| \begin{bmatrix} \mathbf{P} \\ \mathbf{I} \end{bmatrix} x - \begin{bmatrix} \mathbf{v}_1 \\ \mathbf{v}_2 \end{bmatrix} \right|\right|_2^2 \\ &= \frac{\mathbf{P}^T\mathbf{v}_1 + \mathbf{v}_2}{(\mathbf{P}^T\mathbf{P} + \mathbf{I})} \\ &= \frac{\mathbf{H} \circledast \mathbf{v}_1 + \mathbf{v}_2}{\mathbf{H} \circledast \mathbf{H} + \mathbf{1}}\end{aligned} \tag{4.24}$$

where $\mathbf{H}$ is the PSF convolution Kernel.
The addition and division are performed element-wise. The denominator of this operator can be computed beforehand and does not need to be updated with each iteration.

Maximum Likelihood Estimator of Poissonian Noise: $\mathbf{prox}_{\mathbf{p},\rho}$

We now describe the proximal operator for the $\mathbf{w}_1$ update, which is the solution to the Maximum Likelihood Estimator problem. We describe the proximal operator as

$$\mathbf{prox}_{\mathrm{p},\rho}(\mathbf{v}) = \underset{\{\mathbf{w}_1\}}{\operatorname{argmin}}\ J(\mathbf{w}_1) = \underset{\{\mathbf{w}_1\}}{\operatorname{argmin}}\ -\log[p(\mathbf{y}|\mathbf{w}_1)] + \frac{\rho}{2}||\mathbf{v} - \mathbf{w}_1||_2^2$$

where J($\mathbf{w}_1$) is the objective function for the estimator. This function is closely related to the CRLA with the difference in eliminating the need for the PSF matrix $\mathbf{P}$, making the noisy observations independent. Hence, we can take a gradient of the function w.r.t. $\mathbf{w}_1$ element-wise and equate it to zero to obtain the proximal operator.

$$\begin{aligned}\frac{\partial J}{\partial \mathbf{w}_{1_i}} &= -\frac{\mathbf{y}_j}{\mathbf{w}_{1_i}} + 1 + \rho(\mathbf{w}_{1+i} - \mathbf{v}_i) \\ &= \mathbf{w}_{1_i}^2 + \frac{1-\rho\mathbf{v}_i}{\rho}\mathbf{w}_{1_i} - \frac{\mathbf{y}_i}{\rho} = 0\end{aligned}$$

This quadratic equation can be independently solved for each pixel to get the proximal operator. Here, we are only interested in the positive root of the equation. Thus, the proximal operator for $\mathbf{w}_1$ update is given as

$$\mathbf{prox}_{\mathrm{p},\rho}(\mathbf{v}) = -\frac{1-\rho\mathbf{v}}{2\rho} + \sqrt{\left(\frac{1-\rho\mathbf{v}}{2\rho}\right)^2 + \frac{\mathbf{y}}{\rho}} \tag{4.25}$$

Indicator Function: $\mathbf{prox}_{i,\rho}$

The proximal operator for the Indicator function is quite straightforward.

$$\begin{aligned}\mathbf{prox}_{\mathrm{i},\rho}(\mathbf{v}) &= \underset{\{\mathbf{w}_2\}}{\operatorname{argmin}}\ I_{R_+}(\mathbf{w}_2) + \frac{\rho}{2}||\mathbf{v} - \mathbf{w}_2||_2^2 \\ &= \underset{\{\mathbf{w}_2 \in R_+\}}{\operatorname{argmin}} ||\mathbf{v} - \mathbf{w}_2||_2^2 \\ &= \Pi_{R_+}(\mathbf{v})\end{aligned} \tag{4.26}$$

The $\Pi_{R_+}(\cdot)$ is an element-wise projection operator onto the set R_+, given by

$$\Pi_{R_+}(\mathbf{v}_i) = \begin{cases} 0, & \mathbf{v}_i < 0 \\ \mathbf{v}_i, & \mathbf{v}_i \geq 0 \end{cases}$$

We obtain the reconstructed image $\mathbf{x}$ after convergence of iterations in equations 4.23 - 4.26. We use $\rho = 0.001$ for all deconvolutions using ADMM. Altering ρ does not seem to affect the algorithm significantly in our reconstruction. ADMM is typically used for convex function optimization, where convergence is theoretically guaranteed. In our case, the function is convex if $\mathbf{y}_i > 0\ \forall\ i$ (Figueiredo and Bioucas-Dias, 2010). ADMM has been observed to

perform well in certain nonconvex settings as well. In our case, we achieve convergence when applying ADMM to background-subtracted images, along with a reduction in artifacts in the final reconstruction. To enforce the non-negativity constraint, we introduce an additional step in the x-update: $\mathbf{x} = \max\{0, \mathbf{x}\}$. This modification appears to promote sparsity in the reconstructed images. The images reconstructed using ADMM also demonstrate improved recovery of clumps in the image, which we analyze further in the results section.
In the next section, we provide the necessary details regarding the numerical implementation of the convolution algorithms used in this study.

4.5 Numerical Implementation

The preceding section outlined the RL and ADMM algorithms, which rely on efficient numerical techniques for implementation. This section details the key computational methods used in our work which play a crucial role in optimizing the performance and accuracy of the deconvolution process.

Interpolation Before deconvolution, the observed image is first interpolated for RL and ADMM. In this study, we employ Nearest-Neighbor interpolation, as it preserves the original data without introducing new values. In contrast, spline-based interpolation methods, such as bi-cubic interpolation, can introduce artifacts in the reconstructed image. The pixel values are appropriately scaled to preserve the total flux.

Initialization For both RL and ADMM, the initial estimate of the reconstructed image ($\mathbf{x}^0$) is set as a constant, normalized positive matrix. The same initialization is applied to the other variables in ADMM.

FFT Convolve Direct convolution can be used for iterative updates in both RL and ADMM algorithms, offering higher numerical accuracy. However, interpolation significantly increases both the source kernel sizes, making direct convolution computationally expensive and slow. To mitigate this, we employ Fast Fourier Transform (FFT) convolution, which greatly improves processing efficiency. However, FFT convolution introduces boundary effects due to rounding errors in Fourier space. While this issue is less pronounced in ADMM due to sparsity, it leads to artifacts at the edges of the reconstructed image in RL. These artifacts can be substantially reduced by padding the kernel and images, ensuring their impact remains confined to the image boundaries.

Convergence In this work, we use the relative difference as a convergence test for the two algorithms, defined as:

$$\frac{||x^k - x^{k-1}||_2}{||x^{k-1}||_2} \leq \delta \tag{4.27}$$

where δ is taken as 0.001 in our work. For RL, iterations are terminated when this condition is met or when the iteration count reaches 400. However, in ADMM, strict convergence leads to overly compact reconstructions. To address this, we halt ADMM iterations before convergence. Despite early termination, the reconstructed image $\mathbf{x}$ retains details comparable to those obtained with the Richardson-Lucy Algorithm.

To summarize the deconvolution process, we begin with a low-resolution UVIT image that is interpolated to match the pixel scale of HST. The PSF parameters are also scaled appropriately ($\alpha' = \alpha \times \text{scale},\ \beta' = \beta,\ \mathrm{R}'_s = \mathrm{R}_s \times \text{scale}$) to match the updated pixel scale and calculate the sub-pixeling narrower function ($\mathbf{S}$) using a suitable PSF ($\mathbf{R}$) for the new scale. We initialize $\mathbf{x}$ and run the RL and ADMM algorithms till their respective terminating iteration.

In the next chapter, we analyze the reconstructed images from both deconvolution methods and compare their effectiveness.

Chapter 5

Results and Discussion

In this chapter, we present our analysis using the Richardson-Lucy Total Variation (RLTV) and Alternating Direction Method of Multipliers (ADMM) deconvolution algorithms to enhance the resolution of UVIT images. We first model the Point Spread Function (PSF) of the AUDF Deep Field, which is crucial for accurate deconvolution. We then evaluate the performance of RLTV and ADMM by reconstructing surface brightness profiles and recovering clumpy structures in synthetic objects. This analysis is then extended to actual UVIT images to assess the effectiveness of these methods in real observations.

5.1 UVIT PSF

The procedure described for PSF modeling in Chapter 3 has been followed individually for stars selected from the UVIT NUV and FUV filters (2.2.1). In Figure 5.1, we have shown one star from both NUV and FUV filters. The Intensity (I) on the y-axis of the plot for the radial profile has been converted to the AB magnitude scale using the relation: (Borgohain et al., 2022):

$$\mu = -2.5 \log_{10} \frac{I}{\text{pixel-scale}^2} + \text{magZP} \tag{5.1}$$

where magZP is the zero-point of the corresponding filters (2.1).
The exponential profile is the dominant profile of the PSF beyond 5" in both NUV and FUV.

The brightest stars in the samples have a wing extending up to 17" and 14" for NUV and FUV, respectively. The radial profiles in both filters suggest the necessity of modeling the pedestal of the PSF to accurately account for the scattering of light by the instrument.

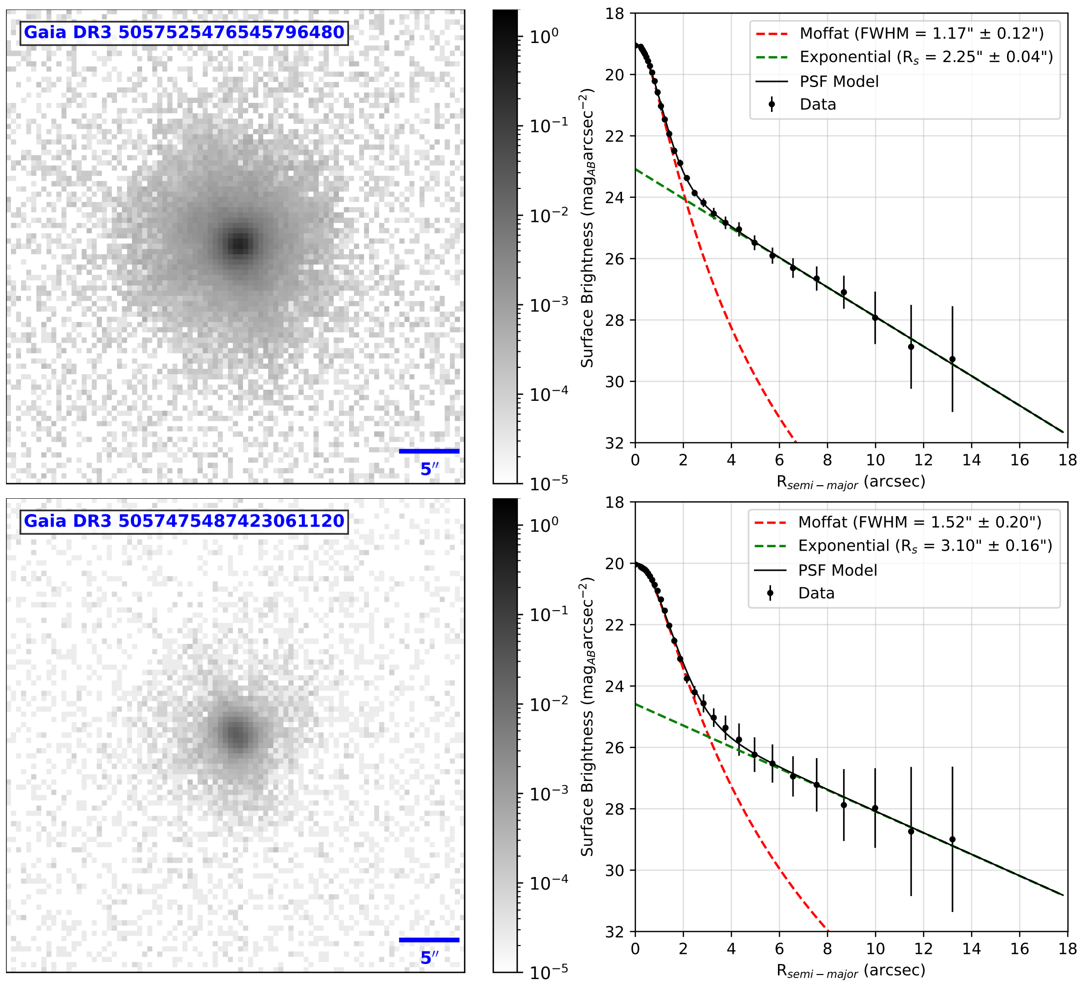

Figure 5.1: NUV (**top**) and FUV stars (**bottom**) PSF Modeling. **Left**: Star Image cutouts The GAIA IDs of the stars are mentioned. **Right**: Plot of 1-D Radial Profiles (black data points) using isophote fitting from Ellipse Task, The Moffat Profile (red dotted curve), Exponential Profile (green dotted curve), and the Total sum of the model profiles (black solid curve).

5.1.1 Fitting Parameters

Figure 5.2 shows the histograms describing the fitting parameters of the Moffat and the Exponential Profiles. Furthermore, the FWHM and R_s histograms showed a normal spread

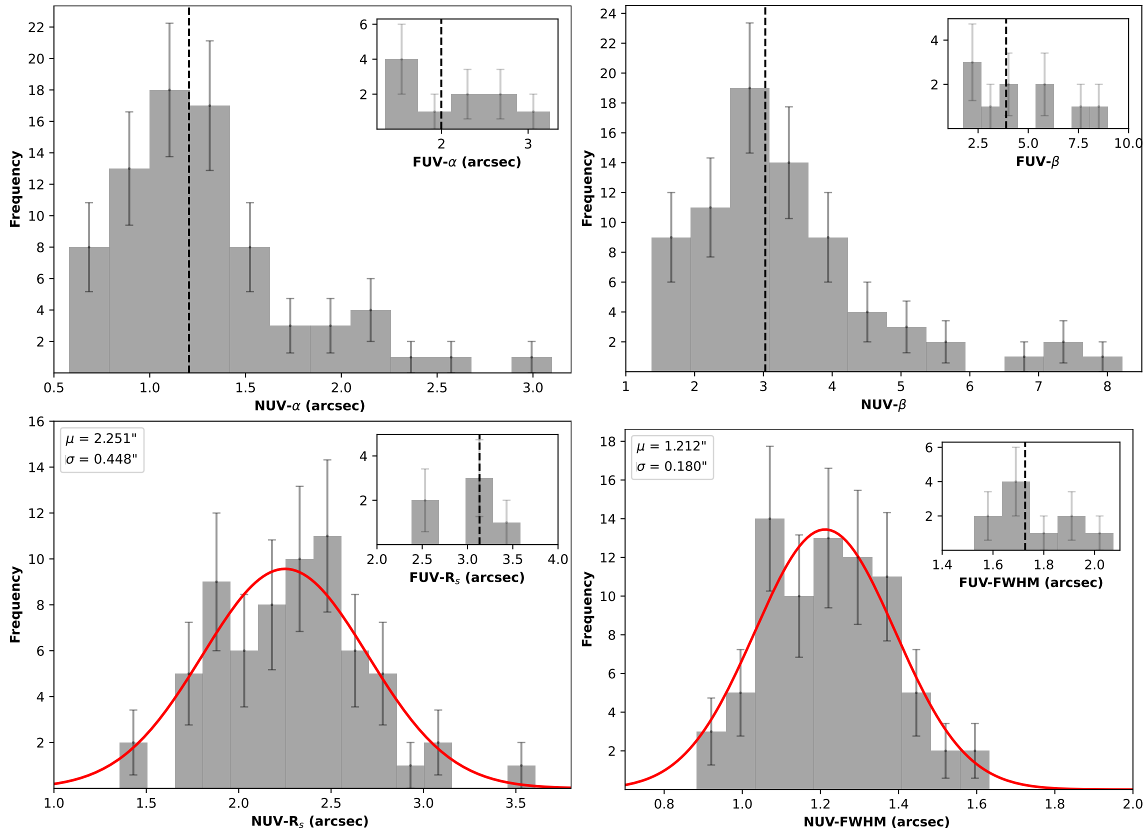

Figure 5.2: Histograms of fitting parameters of Moffat (α, β) and Exponential (R_s) profiles for all the individual stars from the NUV and FUV (inset) filter samples. The bottom right shows the histogram of the calculated FWHM of the Core from the Moffat profile. The dotted black line represents the median of the corresponding samples. The red curve denotes a Gaussian curve fitted to the R_s and FWHM histograms of NUV stars.

and, hence, were fitted with a Gaussian Curve with the least-squares method. We find the median values for the Moffat parameters to be α_{FUV} : 2.00”, β_{FUV}: 3.90 and α_{NUV}: 1.21", β_{NUV}: 3.03. We obtain a median FWHM (equation 3.12) of 1.73" for the F154W channel and a mean FWHM of 1.21" with a standard deviation of 0.18" for the N242W channel. The exponential length scale fitted to the extended pedestal R_s has a median value of 3.13" for F154W and a mean value of 2.25" for N242W with a standard deviation of 0.45".

5.1.2 Ellipticity and Higher Harmonics

The ellipticity $(1-\frac{b}{a})$ of the PSF profiles was computed at the semi-major length of FWHM for individual stars and is shown in the histogram in Figure 5.3. The median ellipticity of

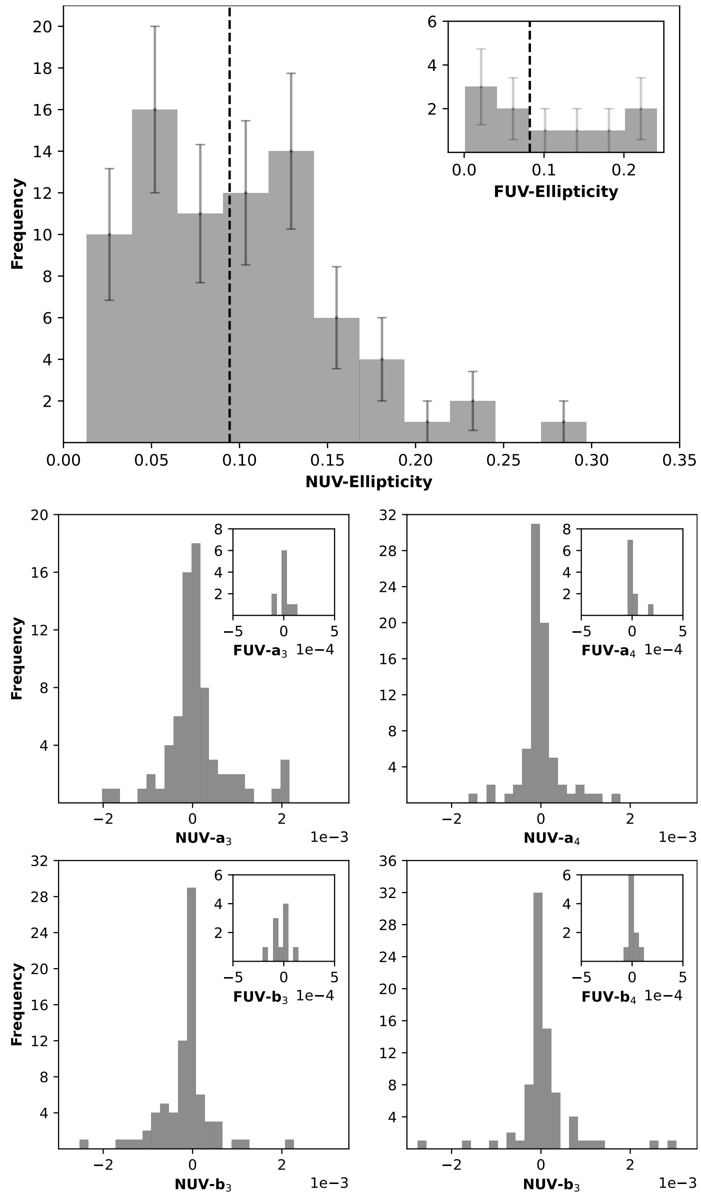

Figure 5.3: **Top**: Histogram of ellipticity of PSF measured at FWHM in NUV and FUV (inset) channels. The median is marked with a black dotted line. **Bottom**: Histograms of coefficients associated with harmonics of order 3,4 for NUV and FUV (inset) channels.

the Stars in NUV and FUV channels is 0.094 and 0.082, respectively.

The histograms for the higher harmonics obtained from the Ellipse Task (3.4), for n = 3,4, are also plotted in Figure 5.3. The histograms for both NUV and FUV samples are distributed around zero. Hence, we can assume the shape of the PSF in UVIT to be smooth with no intrinsic high-frequency components.

5.1.3 Variation in the Field of View

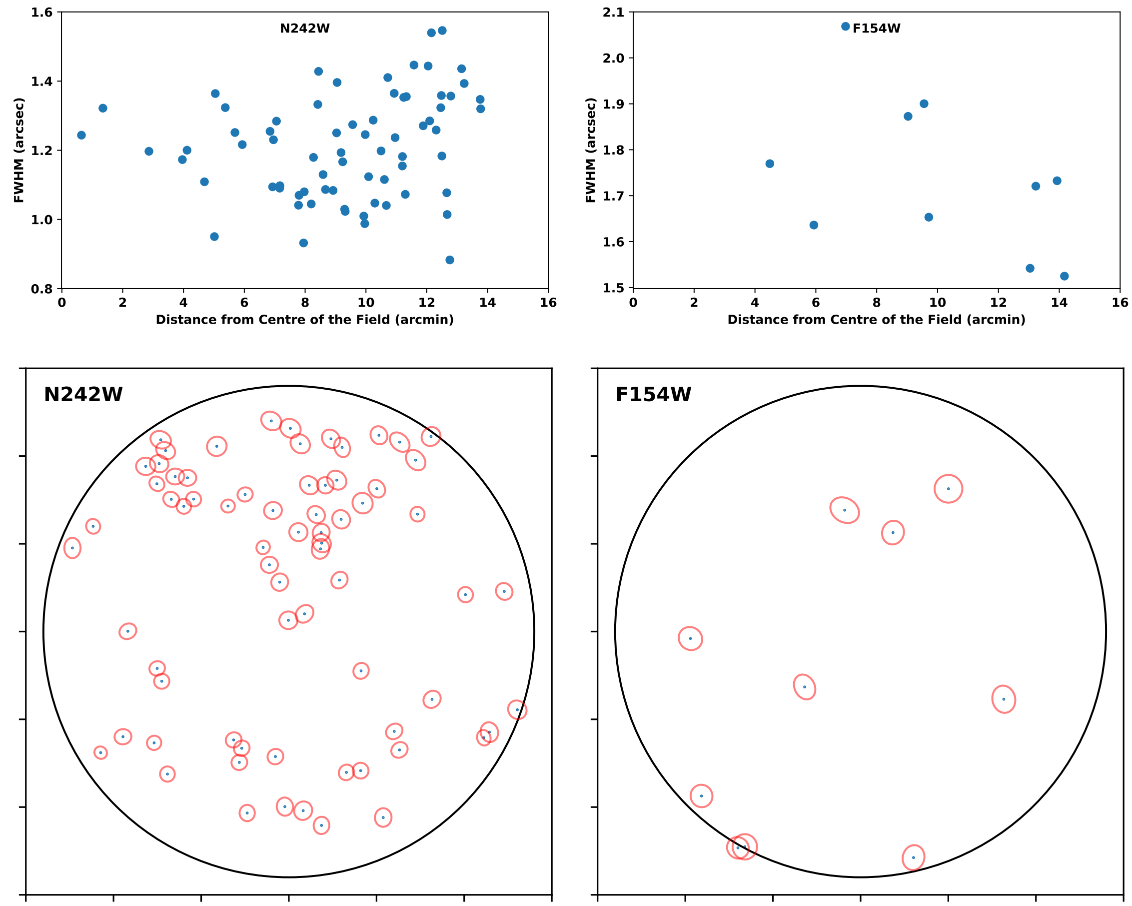

Figure 5.4: **Top**: Variation of Moffat FWHM vs Distance from the Center of the Field for NUV (left) and FUV (right) filters. **Bottom**: Stars selected for the PSF Modeling in NUV (left) and FUV (right) filters in the Field of View (Black Circle: 28' diameter). The ellipses are scaled up by multiplying a constant value by the FWHM of that star. The ellipticity and polar angle are the actual measured values at the semi-major axis of FWHM.

Since the images in AUDF have been taken by an overlap of two fields (CDFS I and CDFS II), we ignore the samples in the overlapping region (7 in NUV, none in FUV) to study the variation of the PSF in the entire FOV. The FWHM doesn't seem to change with the separation from the center. The correlation coefficient between the two is also not significant (~ 0.2 for NUV). A similar trend is observed in ellipticity, except in the top-right corner of the NUV FOV, where ellipticities are higher than in the rest of the field. This aligns with the findings of Tandon, Subramaniam, et al., 2017 for a star cluster.

5.1.4 Stacked Images

To study the curve of growth of the stars in NUV and FUV channels, we utilize mean stacking of images of bright stars, notably 13 stars in NUV (MAG $<$ 19) and 4 in FUV (MAG $<$ 19.5) filters. The PSF of the stacked images is plotted in Figure 5.5. Since the ellipticities of the PSF models are small, we use circular apertures to calculate the curve of growth of the two filters. The radius encircling $\sim 80\%$ of the total flux is found to be 2.46" for NUV and 2.49" for FUV.

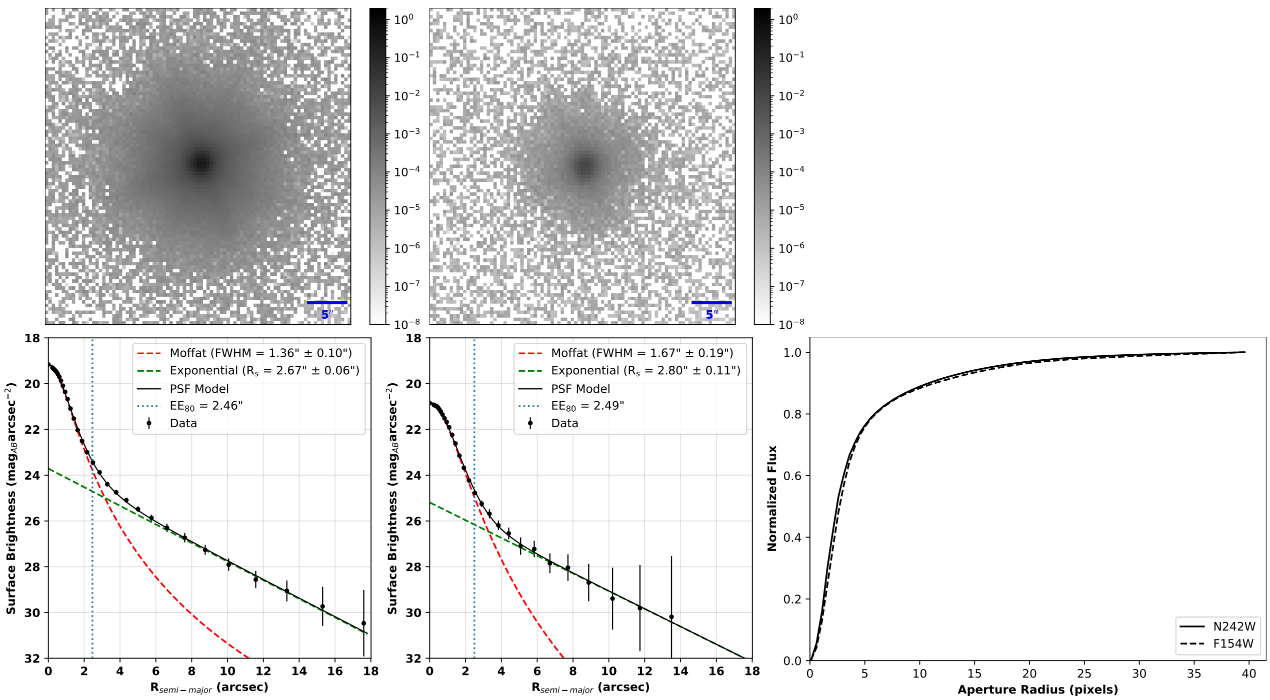

Figure 5.5: PSF Modeling of Stacked cutouts of NUV (**left**) and FUV (**center**) stars. Identical line colors and markers as in Figure 5.1. The blue dotted line represents the radius of 80% Encircled Energy obtained from the Normalized Curve of Growth (**bottom right**) of NUV and FUV channels.

The Point Spread Function (PSF) parameters used for deconvolution are derived from the average values outlined in Section 5.1.1 for NUV images, while for FUV images, the stacked PSF parameters presented in Figure 5.5 are utilized. Since the PSF ellipticity ($<$0.1) has minimal impact on the deconvolution, we adopt a radially symmetric PSF for the process. The results of this deconvolution are presented in the next section.

5.2 Deconvolution of UVIT Images

In this section, we present the results of our deconvolution analysis on UVIT images from the GOODS-South field. We begin with the reconstruction of images in the NUV channel, followed by a selection of FUV images. We first evaluate the effectiveness of these methods using synthetic models, including stars and galaxies, to assess their ability to preserve structural features and photometric accuracy. We then apply these techniques to UVIT observations, examining their impact on resolving clumpy structures and recovering finer details in comparison with corresponding HST images.

5.2.1 CRLA vs MRLA

We have extensively used interpolation in both of the deconvolution techniques. Figure 5.6 presents a comparison in the reconstructions using the Classical versus the Modified Richardson-Lucy Algorithm. A ring-like structure can be inferred from the image reconstructed using CRLA; however, this algorithm introduces substantial artifacts. In contrast, the Modified Richardson-Lucy Algorithm (MRLA) yields better-resolved structures with a significant reduction in artifacts. Given its improved performance in preserving details while minimizing artifacts, MRLA is the preferred choice for reconstruction over CRLA in this study.

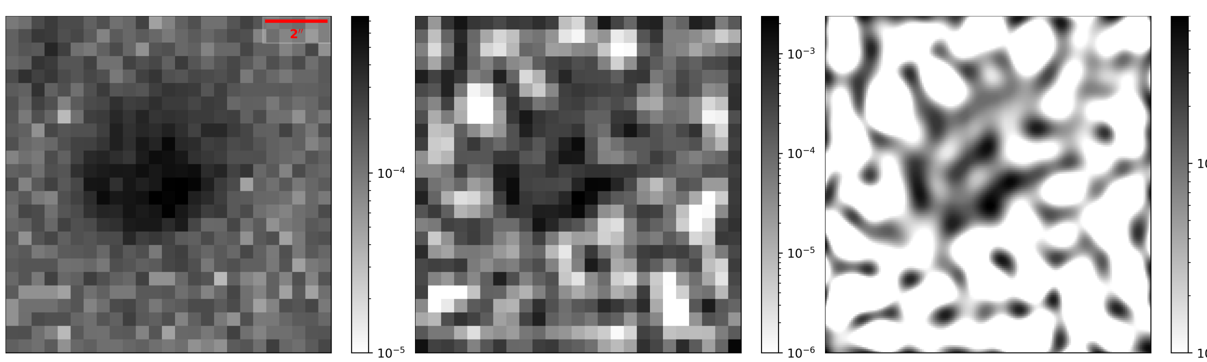

Figure 5.6: Comparison between reconstructed images with and without interpolation. **a)** NUV image of an AGN. Image reconstruction using **b)** Classical Richardson-Lucy Algorithm vs **c)** Modified Richardson-Lucy Algorithm.

5.2.2 Recovery of Synthetic Objects: Stars and Galaxies

We consider a Dirac-delta source for an intrinsic image of the star convolved with the NUV PSF and add Poissonian Noise to construct a synthetic star. The procedure described in Chapter 4 is followed to obtain reconstructed images of the star by the two algorithms. In both reconstructions, the radial spread of the star is reduced to under 7 pixels (correspondingly 1 pixel in UVIT or 0.42") from the UVIT PSF Spread 12"-15". We use the Ellipse Task (3.4) to derive the radial profile of the reconstructed star (5.7). The ADMM profile cuts off at ~ 0.5" and the RL algorithm, on the other hand, gives a continuous profile. We compute the FWHM of the profile obtained from the RL deconvolution to be ~7 pixels (0.42"), which is a threefold improvement over the NUV PSF.

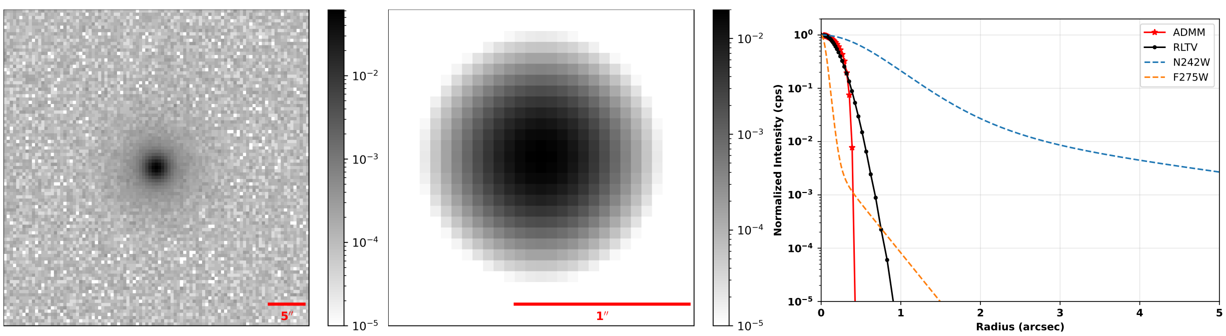

Figure 5.7: Radial Profile of a deconvolved synthetic star. **Left**: Synthetic Star in NUV. **Center**: The deconvolved star using RLTV. **Right**: Normalized Radial Profiles of the star computed using the Ellipse Task for the reconstructions using ADMM (red solid curve) and RLTV (black solid curve). The PSF profiles in HST F275W (yellow dashed curve) and UVIT N242W (blue dashed curve) are given for reference.

To observe the effect of reconstruction on the Surface Brightness Profile, we construct a mock galaxy using a 2-D Sersic profile (R_{eff} =1.2", $n = 2.1$, ellipticity=0.4, $\theta = 1$) at the pixel scale of HST (0.06"). This image is then convolved with scaled UVIT PSF and binned to match the UVIT resolution and a Poissonian noise is added to the image. The image is reconstructed with ADMM and RLTV techniques.

The ADMM algorithm has been used with a background-subtracted test image, but for RLTV, we use an unaltered test image and, therefore, subtract the mean noise value adjusted for the pixel scale from the reconstructed image before running the Ellipse Task. We find that ADMM does not yield a smooth image suitable for modeling the Surface Brightness Profile. This appears to result from the sparsity introduced by the method. RLTV, however, produces a smooth profile that we can model the radial intensity profile of the galaxy. In

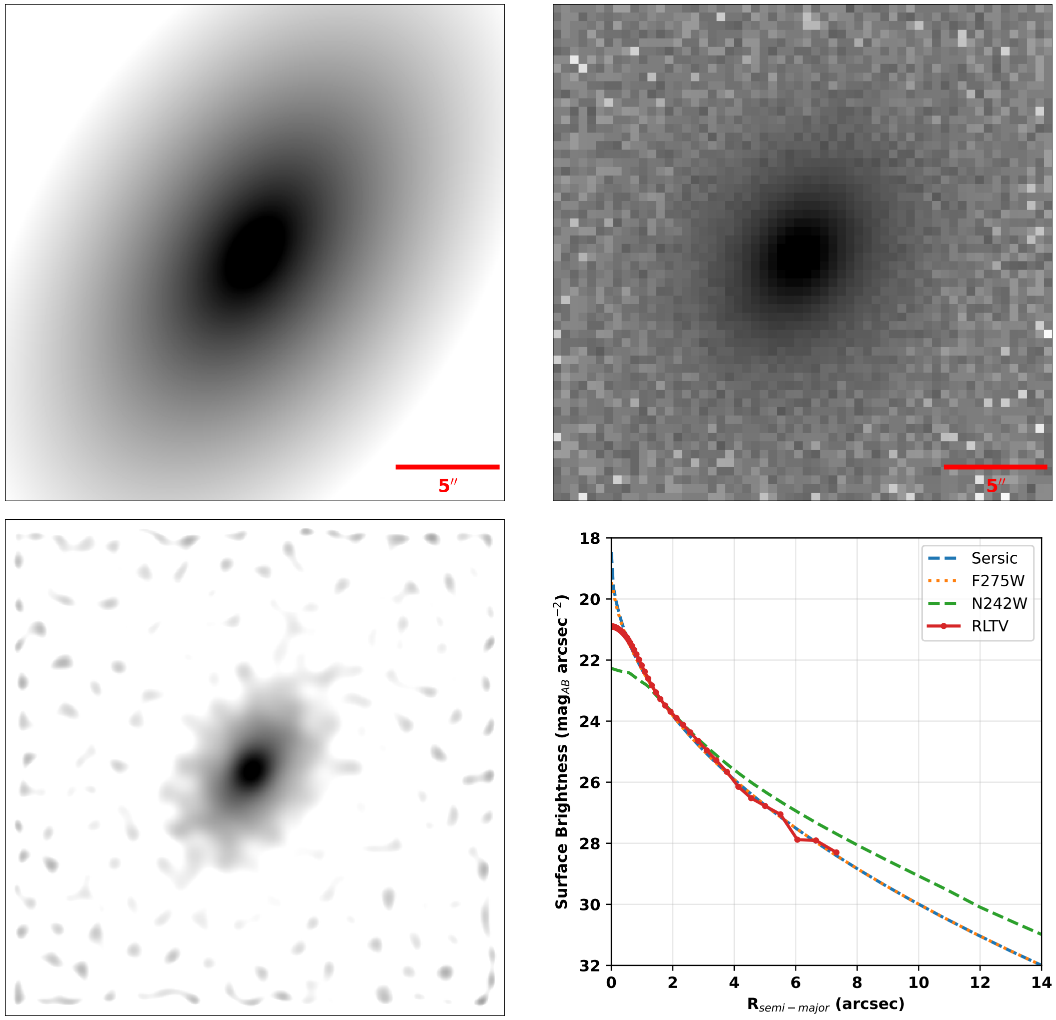

Figure 5.8: Deconvolution of a Synthetic Galaxy with a Sersic Profile. **Top Left**: Synthetic galaxy constructed using a 2-D Sersic Profile. **Top Right**: Test Galaxy image built from the intrinsic image by convolving with UVIT PSF and adding noise. **Bottom Left**: Reconstruction of the Test image with Richardson-Lucy Algorithm. **Bottom Right**: The Radial Profile of the Galaxy. The solid red curve represents the profile of the deconvolved UVIT test image. The intrinsic Sersic (dashed blue curve) and the radial profile in HST F275W (dotted yellow curve) and UVIT N242W (dashed green curve) are given for reference.

the presence of noise, the extent to which the profile can be accurately modeled is reduced, which is expected. As shown in Figure 5.8, the reconstructed galaxy profile appears narrower than the NUV profile. We also verify flux conservation in both techniques by computing the total flux within an ellipse ($e = 0.4$, $\theta = 1$) with a semi-major axis of approximately 7.5", corresponding to the extent of the radial profile. The flux in the RL reconstructed image is $\sim 96\%$ of the intrinsic value, but it varies with the iterations in ADMM. We can thus conclude that ADMM does not necessarily preserve the flux of the reconstructed objects. ADMM decomposes the optimization problem into smaller subproblems, in contrast to RL, which updates the solution in a single global step per iteration. This decomposition may contribute to the lack of flux conservation in ADMM. Introducing a regularization constraint could help enforce flux preservation in the reconstructed images.

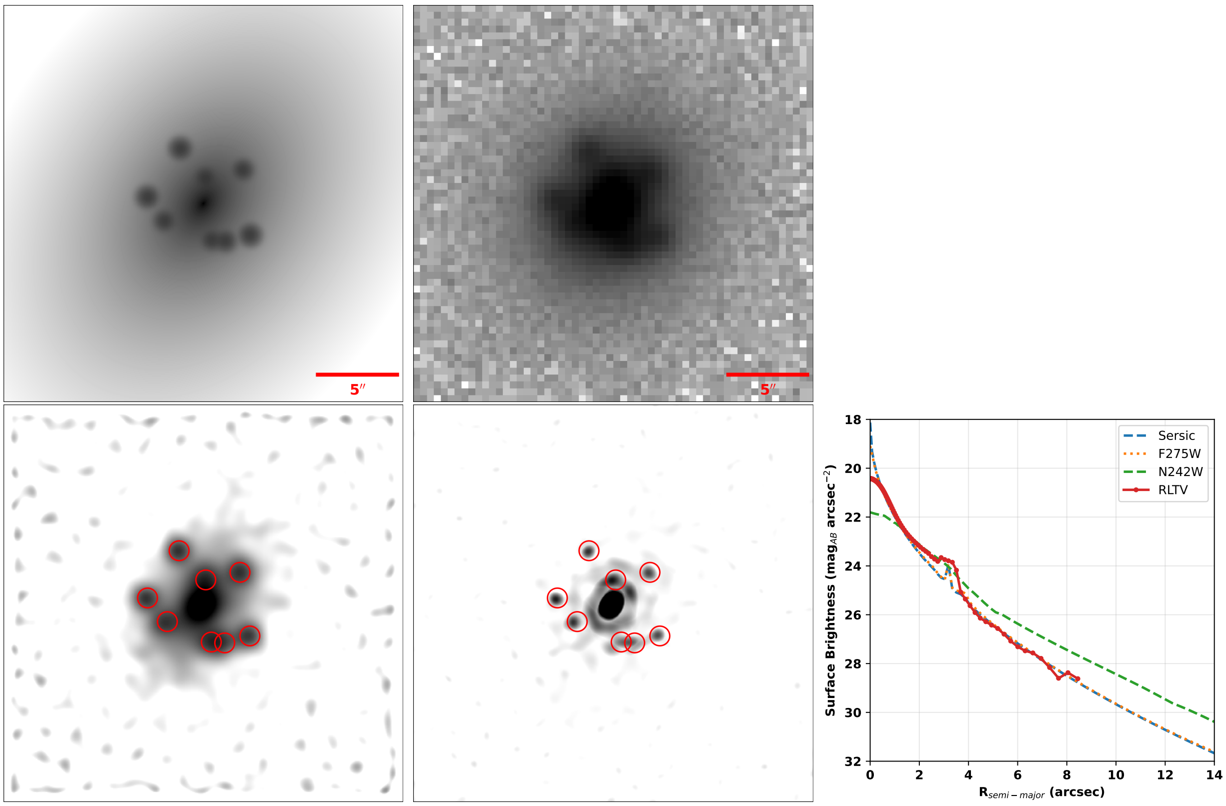

Figure 5.9: Deconvolution of a Synthetic Clumpy Galaxy. **Top Left**: Synthetic galaxy constructed using a 2-D Sersic Profile and Gaussian Clumps. **Top Center**: UVIT Test galaxy image. **Bottom Left**: Reconstruction of the Test image with Richardson-Lucy Algorithm.**Bottom Center**: Reconstruction of the Test image with ADMM. In both images, the circular apertures are the positions of the clumps in the intrinsic image. **Bottom Right**: The Radial Profile of the Galaxy from the Ellipse Task. Identical line colors and markers as in Figure 5.8

To study the effectiveness of the algorithms for feature recovery, we construct a clumpy mock galaxy with a 2-D Sersic Profile (R_{eff} =1.2", $n = 2.1$, ellipticity=0.3, $\theta = 1$) and 8 Gaussian Clumps ($\sigma = 0.3$" (5 pixels)) spread throughout the structure. Similar to the previous galaxy, we deconvolve the image using RLTV and ADMM and plot a Surface Brightness Profile (Figure 5.9). The reconstructed images exhibit a clear improvement over the test image. In the UVIT Test image, visually, we can only differentiate 4 out of the total 8 clumps. In RLTV and ADMM, we can differentiate 6 and 7 of the original clumps respectively. Two closely spaced clumps in the intrinsic image remain unresolved in both reconstructions. However, ADMM appears to outperform RLTV in resolving clumpy structures, particularly evident in the marked clump near the galaxy center. We also observe a few false positives due to artifacts in ADMM, particularly near the center, which we might be able to suppress with an appropriate regularization term. The Surface Brightness Profile of the galaxy exhibits a trend consistent with the previous case. A notable difference is the effect of the clumps in the profile. In the intrinsic and HST-convolved profiles (with small FWHM), a distinct and sharp kink is observed at the location of the clumps, unlike the UVIT test image, which smooths over the profile. The profile derived from RLTV also exhibits a noticeable bump at the same location, which suggests it better recovers the localized variations in surface brightness.

Having completed the analysis of synthetic figures, we now examine the reconstructions of selected objects observed by UVIT in the NUV and FUV filters.

5.2.3 Reconstruction of Observed UVIT Images

In this section, we present the reconstructed images of UVIT objects in GOODS-South. We first analyze the deconvolution results for images taken in the NUV channel, followed by those in the FUV channel.

The UVIT image in Figure 5.10 consists of two marginally resolved stars in the NUV channel. As both sources are bright with high SNR, we are able to reconstruct well-resolved images with almost negligible artifacts. The separation between the two sources is also consistent with the HST F275W observation.

The deconvolution of the UVIT image in Figure 5.11 yields a high-quality reconstruction of the galaxy. Both RLTV and ADMM successfully reveal the spiral structure, and a considerable number of clumps (marked with red circles) are recovered in locations consistent with those in the HST image. While the HST image retains more distinct clumps due to its higher resolution, the deconvolution results demonstrate a substantial improvement over the original UVIT image. We also plot the Surface Brightness Profile for the UVIT, HST, and RLTV images. The profile exhibits a similar trend to that observed in the clumpy synthetic

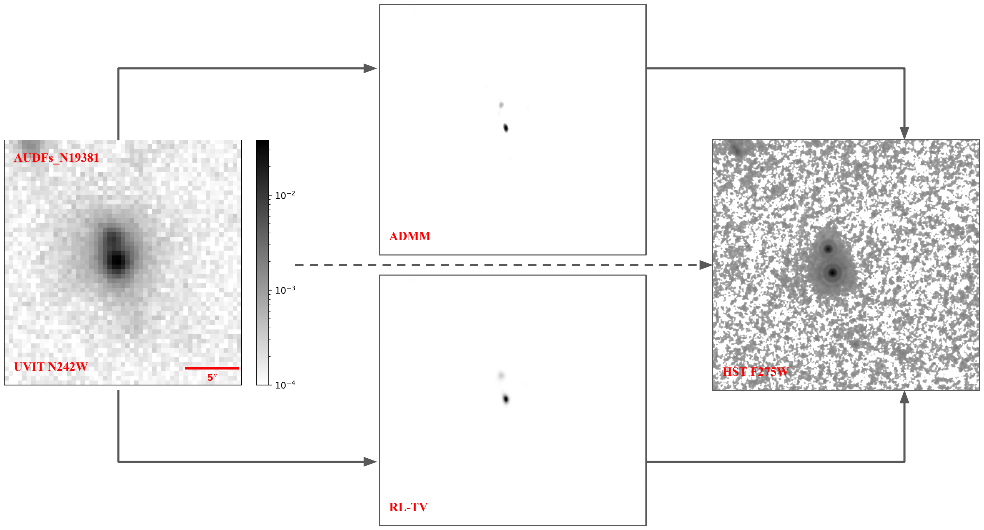

Figure 5.10: Deconvolution of Two Marginally Resolved Stars in the N242W Filter. The UVIT image (**Left**), reconstructed using the Richardson-Lucy algorithm (**Center Top**) and the ADMM technique (**Center Bottom**), successfully resolves the two sources into distinct sources. The HST F275W image (**Right**) is given for comparison. The UVIT ID of the central object is mentioned.

galaxy. The reconstructed image profile is narrower and more irregular, resembling the HST profile for clumpy galaxies, in contrast to the smoother profile observed in the UVIT image.

The reconstruction of the galaxy AUDFs_N02608 (Figure 5.12)in the NUV filter shows a significant improvement over the UVIT image. A bright clump is visible in both RLTV and ADMM reconstructions, corresponding to a similar feature in the HST F275W image. However, ADMM more effectively resolves the clumpy features observed in the HST images compared to RLTV.

Figure 5.13 demonstrates the effectiveness of the reconstruction in resolving clumps. We have used `unsharp_mask` to enhance the clumps for better detection by `SExtractor`. Both algorithms demonstrate a substantial improvement in resolving clumpy structures compared to the original UVIT images, which suffer from significant blurring due to the UVIT's broad PSF. The deconvolved images recover a number of clumps that are otherwise indistinguishable in the observed data. Among the two, ADMM particularly stands out, resolving a noticeably higher number of distinct clumps and recovering finer morphological features with fewer artifacts than RLTV. However, it is important to note that the HST images still reveal a greater number of clumps, owing to their superior resolution. Additionally, in the reconstructed images, large artifacts may sometimes be misidentified as clumps, which

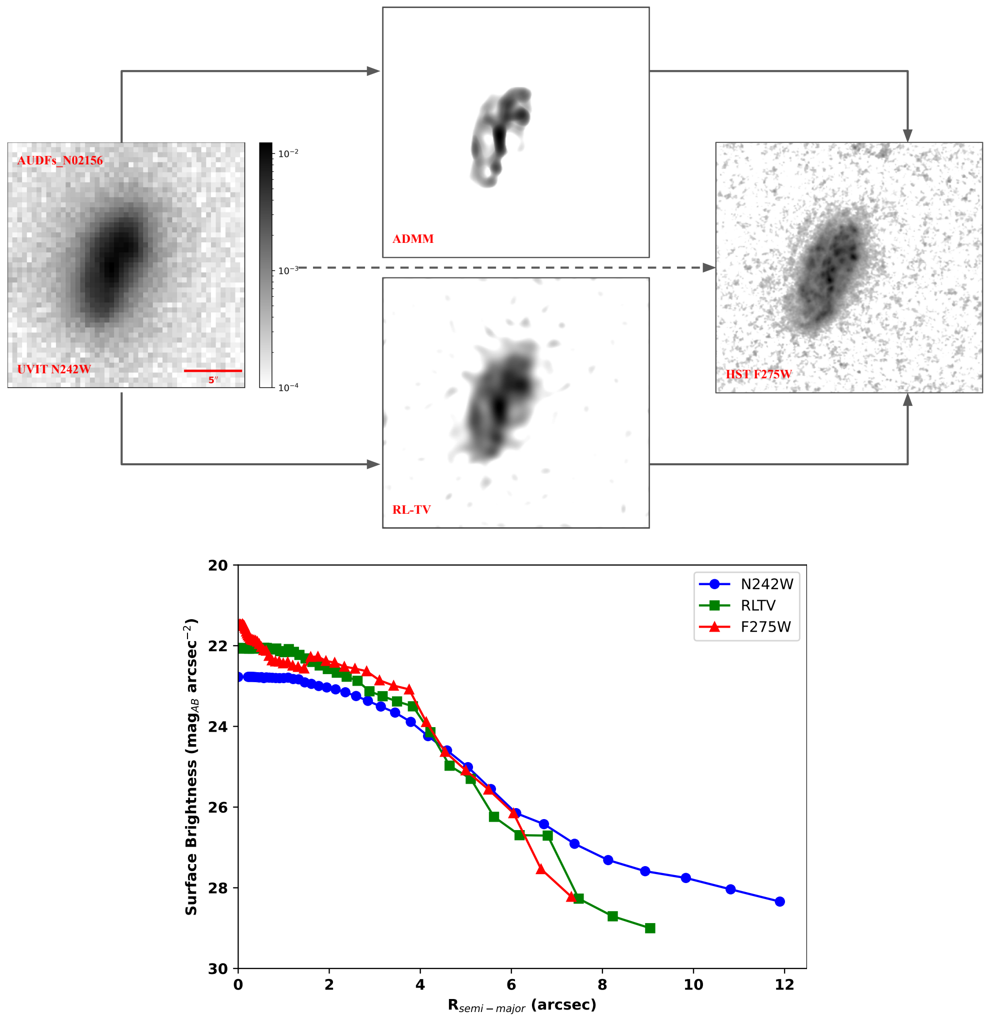

Figure 5.11: Deconvolution of a Galaxy (ID: AUDFs_N02156)) (**Top**). The reconstructed images allow for a clearer identification of the galaxy's spiral morphology. Surface Brightness Profile of the galaxy obtained from the Ellipse task (**Bottom**) from the UVIT N242W (blue curve), HST F275W (red curve), and the RLTV reconstructed (green curve) images.

should be taken into consideration when interpreting the clumps. We have given a few more image reconstructions as examples, which demonstrate the usefulness of the two algorithms in identifying mergers, etc. The RLTV and ADMM reconstructions of AUDFs_N01194 (Figure 5.14) exhibit a structure comparable to the HST image. The unusual shape recovered in this case suggests a merger of galaxies. Indeed, we find 4 galaxies at the same redshift ($z \sim 0.23$), which also points towards a merger. However, the RLTV reconstruction contains significant artifacts. In this case, ADMM can be used as a reference to identify and exclude artifacts while studying the photometric features of the galaxy from the RLTV image.

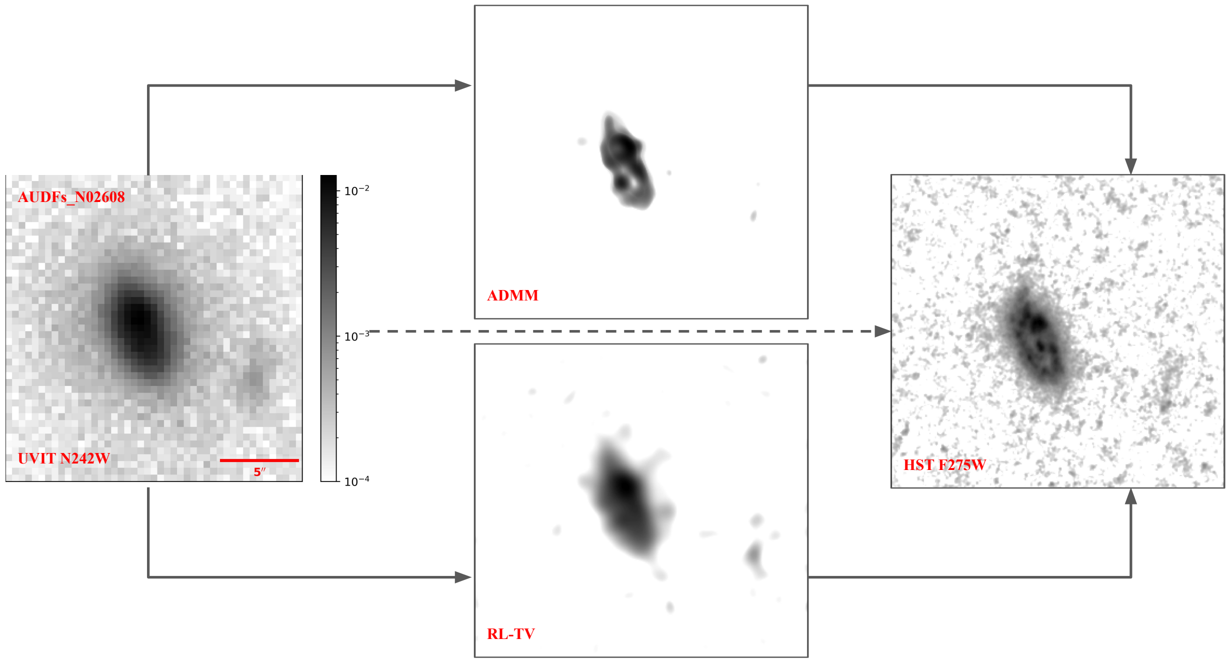

Figure 5.12: Deconvolution of a Galaxy (ID: AUDFs_N02608)). Both RLTV and ADMM produce well-resolved images of the galaxy, with ADMM more effectively capturing the clumpy structure, aligning more closely with the HST image.

FUV images are often highly noisy, making morphological analysis challenging. However, they provide valuable information on star-forming regions and potential Lyman Continuum (LyC) leakers, offering critical insights into galaxy evolution and reionization.

The reconstruction of the FUV object AUDFs_F11355 (Figure 5.15) may aid in identifying star-forming regions. Due to the lack of high-quality HST coverage in bands near F154W for the GOODS-South Field, we include the F275W image solely for reference and for aligning the positions of the clumps.

The deconvolved images of Galaxy (AUDFs_F13631) primarily reveal a collection of bright clumps. Mapping their positions onto the HST image confirms that these clumps are located along the spiral arms, suggesting that this region is a strong candidate for active star formation, as star formation in spiral galaxies typically occurs in the arms.

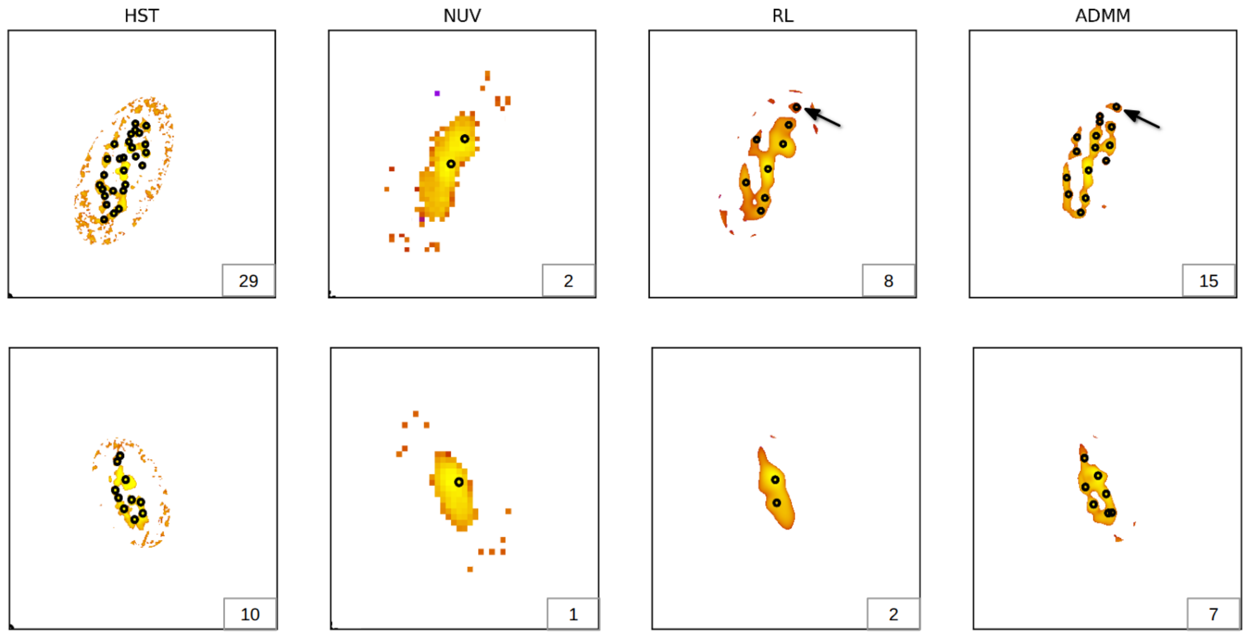

Figure 5.13: Clumps in galaxies AUDFs_N02156 (**top**) and AUDFs_N02608 (**bottom**) in HST, NUV and reconstructed images. The number of clumps detected is indicated in the box at the bottom right of each image. Aside from the artifacts (marked with a black arrow), ADMM successfully resolves a significantly greater number of clumps compared to RLTV.

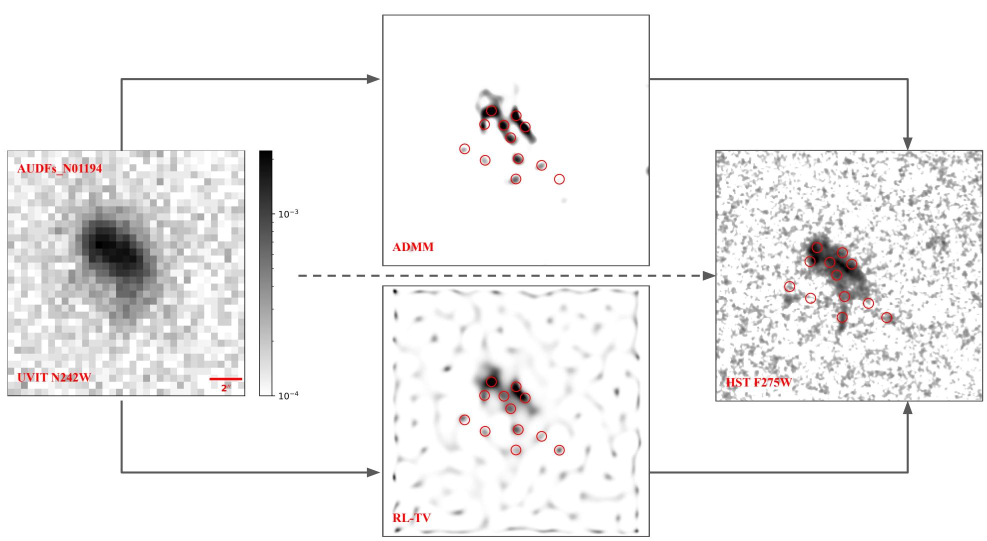

Figure 5.14: Deconvolution of a Galaxy (ID: AUDFs_N01194). The overall morphology recovered by both deconvolution techniques closely resembles the HST image. The red circles are the prominent clumps identified visually with DS9 in reconstructed images. However, the RLTV reconstruction exhibits more artifacts compared to ADMM.

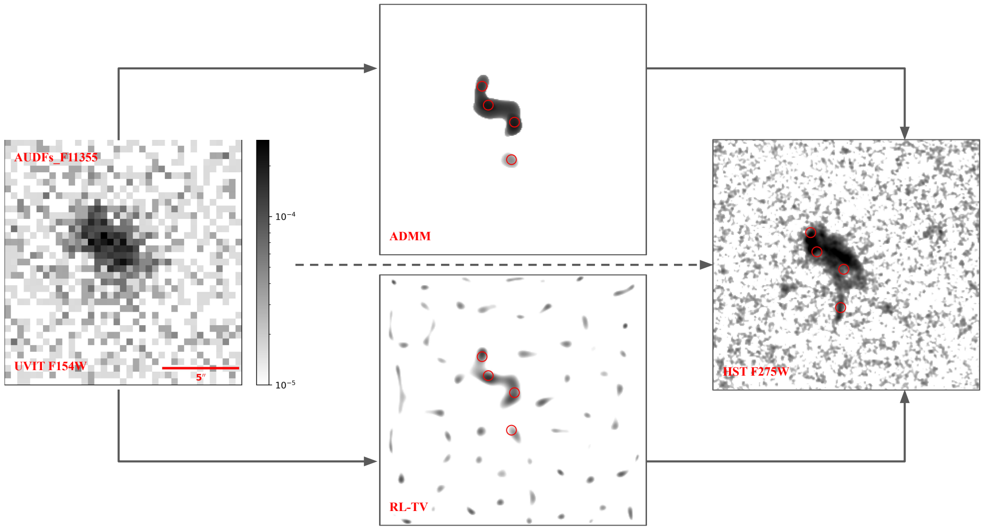

Figure 5.15: Deconvolution of a Galaxy (ID: AUDFs_F11355) (same as NUV object AUDFs_N01194). The marked clumps may indicate potential star-forming regions.

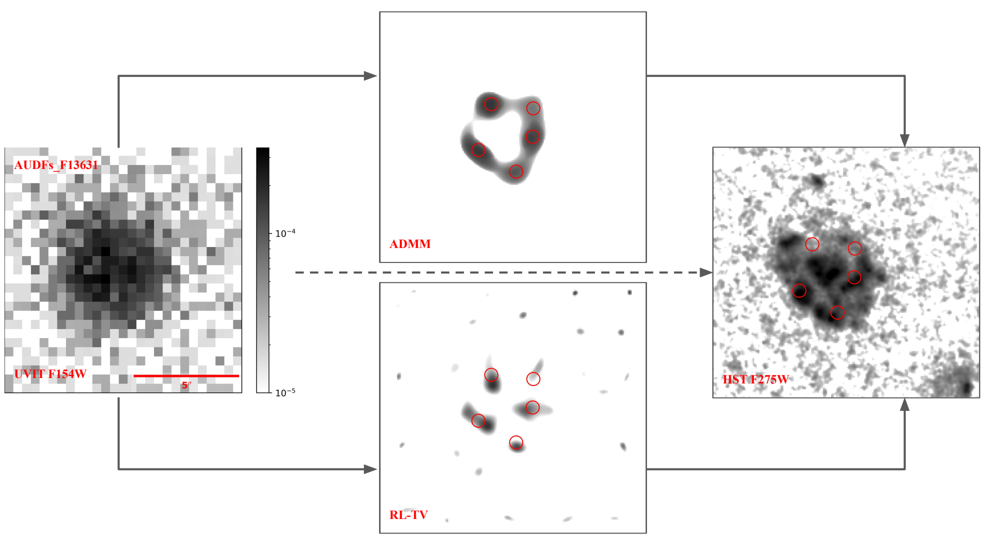

Figure 5.16: Deconvolution of a Galaxy (ID: AUDFs_F13631). The recovered clumps (red circles) are present in the spiral arms of the galaxy in the HST image.

Chapter 6

Conclusion and Outlook

This work focused on improving the resolution of UVIT images using deconvolution techniques. We employed the Richardson-Lucy (RL) deconvolution and the Alternating Direction Method of Multipliers (ADMM) to reconstruct images and recover finer morphological details.

We first modeled the PSF of stars observed in the NUV and FUV filters, providing insights into the PSF characteristics and confirming the absence of higher-frequency components. Additionally, we analyzed PSF variations across the field of view, which will be beneficial for future studies involving PSF-dependent corrections in UVIT data.

The Richardson-Lucy algorithm conserves flux and can be reliably used for photometric analysis. Surface Brightness Profiles derived from synthetic galaxy models show a considerable improvement compared to UVIT profiles. ADMM, on the other hand, does not conserve flux, making it unsuitable for photometric analysis, but it excels at recovering clumps and morphological features with fewer artifacts than RL.

A hybrid approach utilizing RL for photometry while leveraging ADMM for morphological analysis may provide the best of both methods in future studies, enabling a more comprehensive understanding of galaxy structures and star-forming regions.

6.1 Future Direction

We can extend this study by exploring other deep fields with FUV coverage from HST to further analyze and refine the deconvolution of F154W images. A significant portion of the CDFS and GOODS-South remains unsurveyed by HST and JWST. The deconvolution techniques developed here will contribute to future studies across multiple wavelengths, improving our ability to analyze galaxy morphology and structure in deep-field surveys.
ADMM is a widely used algorithm in image processing, but its application in astronomy remains relatively unexplored. There is potential for further development, particularly by incorporating additional regularization constraints to enforce flux conservation. Additionally, machine learning techniques can be leveraged to utilize publicly available datasets for training and improving deconvolution methods.
Deconvolution, being an inherently ill-posed problem, allows room for further refinement; thus, there is scope for developing more robust and advanced algorithms to achieve improved image reconstruction and higher resolution.

Data and Software Acknowledgment

This work utilizes data from the AstroSat mission, developed by the Indian Space Research Organisation (ISRO), and archived at the Indian Space Science Data Centre (ISSDC). The Far-Ultraviolet (FUV) and Near-Ultraviolet (NUV) observations were conducted using the UVIT, developed through a collaboration between the Indian Institute of Astrophysics (IIA), the Inter-University Centre for Astronomy and Astrophysics (IUCAA), the Tata Institute of Fundamental Research (TIFR), ISRO, and the Canadian Space Agency (CSA).
We extensively used Python 3 (Python Core Team, 2023) for data processing and analysis. We acknowledge the Python community and the developers of various open-source libraries, including NumPy (Harris et al., 2020) and SciPy (Virtanen et al., 2020) for numerical computations, Matplotlib (Hunter, 2007) for visualization, Astropy (Astropy Collaboration et al., 2022) for astronomical data analysis, and Photutils (Bradley et al., 2024) and `SExtractor` (Bertin and Arnouts, 1996) for source detection and photometry. Additionally, we acknowledge the use of SAOImage-DS9 (Smithsonian Astrophysical Observatory, 2000) for image visualization.

Bibliography

[1] Jay Anderson and Ivan R. King. "Toward High-Precision Astrometry with WFPC2. I. Deriving an Accurate Point-Spread Function". In: 112.776 (Oct. 2000), pp. 1360–1382. DOI: 10.1086/316632. arXiv: astro-ph/0006325 [astro-ph].

[2] Astropy Collaboration, Adrian M. Price-Whelan, Pey Lian Lim, et al. "The Astropy Project: Sustaining and Growing a Community-oriented Open-source Project and the Latest Major Release (v5.0) of the Core Package". In: 935.2, 167 (Aug. 2022), p. 167. DOI: 10.3847/1538-4357/ac7c74. arXiv: 2206.14220 [astro-ph.IM].

[3] E. Bertin and S. Arnouts. "SExtractor: Software for source extraction." In: 117 (June 1996), pp. 393–404. DOI: 10.1051/aas:1996164.

[4] Anshuman Borgohain, Kanak Saha, Bruce Elmegreen, et al. "Extended far-ultraviolet emission in distant dwarf galaxies". In: 607.7919 (July 2022), pp. 459–462. DOI: 10.1038/s41586-022-04905-9. arXiv: 2207.10708 [astro-ph.GA].

[5] Stephen Boyd, Neal Parikh, Eric Chu, Borja Peleato, and Jonathan Eckstein. "Distributed Optimization and Statistical Learning via the Alternating Direction Method of Multipliers". In: *Foundations and Trends® in Machine Learning* 3.1 (2011), pp. 1–122. ISSN: 1935-8237. DOI: 10.1561/2200000016. URL: http://dx.doi.org/10.1561/2200000016.

[6] Ronald N. Bracewell. *The Fourier transform and its applications*. 2000.

[7] Larry Bradley, Brigitta Sipőcz, Thomas Robitaille, et al. *astropy/photutils: 2.0.2*. Version 2.0.2. Oct. 2024. DOI: 10.5281/zenodo.13989456. URL: https://doi.org/10.5281/zenodo.13989456.

[8] T. J. Cornwell and K. F. Evans. "A simple maximum entropy deconvolution algorithm". In: 143.1 (Feb. 1985), pp. 77–83.

[9] Ashish Devaraj, Prajwel Joseph, CS Stalin, Shyam N Tandon, and Swarna K Ghosh. "UVIT Observations of the Small Magellanic Cloud: Point-source Catalog". In: *The Astrophysical Journal* 946.2 (2023), p. 65.

[10] Nicolas Dey, Laure Blanc-Feraud, Christophe Zimmer, et al. "Richardson–Lucy algorithm with total variation regularization for 3D confocal microscope deconvolution". In: *Microscopy research and technique* 69.4 (2006), pp. 260–266. DOI: 10.1002/jemt.20294.

[11] Mário A. T. Figueiredo and José M. Bioucas-Dias. "Restoration of Poissonian Images Using Alternating Direction Optimization". In: *IEEE Transactions on Image Processing* 19.12 (Dec. 2010), pp. 3133–3145. DOI: 10.1109/TIP.2010.2053941. arXiv: 1001.2244 `[math.OC]`.

[12] B. R. Frieden. "Restoring astronomical objects using maximum entropy." In: *Journal of the Optical Society of America (1917-1983)* 68 (Jan. 1978), p. 1375.

[13] Gaia Collaboration, A. G. A. Brown, A. Vallenari, et al. "Gaia Early Data Release 3. Summary of the contents and survey properties". In: 649, A1 (May 2021), A1. DOI: 10.1051/0004-6361/202039657. arXiv: 2012.01533 `[astro-ph.GA]`.

[14] Charles R Harris, K Jarrod Millman, Stéfan J van der Walt, et al. "Array programming with NumPy". In: *Nature* 585.7825 (2020), pp. 357–362. ISSN: 1476-4687. DOI: 10.1038/s41586-020-2649-2. URL: https://doi.org/10.1038/s41586-020-2649-2.

[15] J. A. Högbom. "Aperture Synthesis with a Non-Regular Distribution of Interferometer Baselines". In: 15 (June 1974), p. 417.

[16] John D Hunter. "Matplotlib: A 2D graphics environment". In: *Computing in science & engineering* 9.3 (2007), p. 90.

[17] Raúl Infante-Sainz, Ignacio Trujillo, and Javier Román. "The Sloan Digital Sky Survey extended point spread functions". In: 491.4 (Feb. 2020), pp. 5317–5329. DOI: 10.1093/mnras/stz3111. arXiv: 1911.01430 `[astro-ph.IM]`.

[18] Robert I. Jedrzejewski. "CCD surface photometry of elliptical galaxies - I. Observations, reduction and results." In: 226 (June 1987), pp. 747–768. DOI: 10.1093/mnras/226.4.747.

[19] Amit Kumar, S. K. Ghosh, J. Hutchings, et al. "Ultra Violet Imaging Telescope (UVIT) on ASTROSAT". In: *Space Telescopes and Instrumentation 2012: Ultraviolet to Gamma Ray*. Ed. by Tadayuki Takahashi, Stephen S. Murray, and Jan-Willem A. den Herder. Vol. 8443. Society of Photo-Optical Instrumentation Engineers (SPIE) Conference Series. Sept. 2012, 84431N, 84431N. DOI: 10.1117/12.924507. arXiv: 1208.4670 [astro-ph.IM].

[20] Xiangyu Li, Xin Zhang, Chaolin Fan, et al. "Deconvolution based on sparsity and continuity improves the quality of ultrasound image". In: *Computers in Biology and Medicine* 169 (2024), p. 107860. ISSN: 0010-4825. DOI: https://doi.org/10.1016/j.compbiomed.2023.107860. URL: https://www.sciencedirect.com/science/article/pii/S0010482523013252.

[21] L. B. Lucy. "An iterative technique for the rectification of observed distributions". In: 79 (June 1974), p. 745. DOI: 10.1086/111605.

[22] A. F. J. Moffat. "A Theoretical Investigation of Focal Stellar Images in the Photographic Emulsion and Application to Photographic Photometry". In: 3 (Dec. 1969), p. 455.

[23] K. Nkashima and H. Takami. "Deconvolution of Sub-Pixeled Richardson-Lucy Algorithm". In: *European Southern Observatory Conference and Workshop Proceedings*. Ed. by Domenico Bonaccini. Vol. 56. European Southern Observatory Conference and Workshop Proceedings. Jan. 1999, p. 323.

[24] H. Nyquist. "Certain Topics in Telegraph Transmission Theory". In: *Transactions of the American Institute of Electrical Engineers* 47.2 (Apr. 1928), pp. 617–624. DOI: 10.1109/T-AIEE.1928.5055024.

[25] Python Core Team. *Python: A dynamic, open source programming language*. Python version 3.12. Python Software Foundation. 2023. URL: https://www.python.org/.

[26] Marc Rafelski, Harry I Teplitz, Jonathan P Gardner, et al. "UVUDF: ultraviolet through near-infrared catalog and photometric redshifts of galaxies in the Hubble Ultra Deep Field". In: *The Astronomical Journal* 150.1 (2015), p. 31.

[27] William Hadley Richardson. "Bayesian-Based Iterative Method of Image Restoration". In: *Journal of the Optical Society of America (1917-1983)* 62.1 (Jan. 1972), p. 55.

[28] Leonid I. Rudin, Stanley Osher, and Emad Fatemi. "Nonlinear total variation based noise removal algorithms". In: *Physica D Nonlinear Phenomena* 60.1-4 (Nov. 1992), pp. 259–268. DOI: 10.1016/0167-2789(92)90242-F.

[29] Kanak Saha, Suraj Dhiwar, Sudhanshu Barway, Chaitra Narayan, and Shyam Tandon. "The central region of the enigmatic Malin 1". In: *Journal of Astrophysics and Astronomy* 42.2, 59 (Oct. 2021), p. 59. DOI: 10.1007/s12036-021-09715-5. arXiv: 2101.07002 [astro-ph.GA].

[30] Kanak Saha, Soumil Maulick, Pushpak Pandey, et al. "The AstroSat UV Deep Field South. I. Far- and Near-ultraviolet Source Catalog of the GOODS South Region". In: 275.2, 28 (Dec. 2024), p. 28. DOI: 10.3847/1538-4365/ad7e2a. arXiv: 2408.03629 [astro-ph.GA].

[31] Yusuke Sakai, Shinya Yamada, Toshiki Sato, et al. "Richardson-Lucy Deconvolution with a Spatially Variant Point-spread Function of Chandra: Supernova Remnant Cassiopeia A as an Example". In: 951.1, 59 (July 2023), p. 59. DOI: 10.3847/1538-4357/acd9b3. arXiv: 2306.13355 [astro-ph.HE].

[32] Takatoshi Shibuya, Noriaki Miura, Kenji Iwadate, et al. "Galaxy morphologies revealed with Subaru HSC and super-resolution techniques. I. Major merger fractions of L_{UV} 3-15 L^*_{UV} dropout galaxies at $z \sim$ 4-7". In: 74.1 (Feb. 2022), pp. 73–91. DOI: 10.1093/pasj/psab111. arXiv: 2106.03728 [astro-ph.GA].

[33] Smithsonian Astrophysical Observatory. *SAOImage DS9: A utility for displaying astronomical images in the X11 window environment.* Astrophysics Source Code Library, record ascl:0003.002. Mar. 2000.

[34] J. L. Starck, E. Pantin, and F. Murtagh. "Deconvolution in Astronomy: A Review". In: 114.800 (Oct. 2002), pp. 1051–1069. DOI: 10.1086/342606.

[35] Peter B. Stetson. "DAOPHOT: A Computer Program for Crowded-Field Stellar Photometry". In: 99 (Mar. 1987), p. 191. DOI: 10.1086/131977.

[36] S. N. Tandon, J. B. Hutchings, S. K. Ghosh, et al. "In-orbit Performance of UVIT and First Results". In: *Journal of Astrophysics and Astronomy* 38.2, 28 (June 2017), p. 28. DOI: 10.1007/s12036-017-9445-x. arXiv: 1612.00612 [astro-ph.IM].

[37] S. N. Tandon, J. Postma, P. Joseph, et al. "Additional Calibration of the Ultraviolet Imaging Telescope on Board AstroSat". In: 159.4, 158 (Apr. 2020), p. 158. DOI: 10.3847/1538-3881/ab72a3. arXiv: 2002.01159 [astro-ph.IM].

[38] S. N. Tandon, Annapurni Subramaniam, V. Girish, et al. "In-orbit Calibrations of the Ultraviolet Imaging Telescope". In: 154.3, 128 (Sept. 2017), p. 128. DOI: 10.3847/1538-3881/aa8451. arXiv: 1705.03715 [astro-ph.IM].

[39] Pauli Virtanen, Ralf Gommers, Travis E. Oliphant, et al. "SciPy 1.0: Fundamental Algorithms for Scientific Computing in Python". In: *Nature Methods* (2020). DOI: https://doi.org/10.1038/s41592-019-0686-2.

[40] Katherine E. Whitaker, Mohammad Ashas, Garth Illingworth, et al. "The Hubble Legacy Field GOODS-S Photometric Catalog". In: 244.1, 16 (Sept. 2019), p. 16. DOI: 10.3847/1538-4365/ab3853. arXiv: 1908.05682 [astro-ph.GA].